Cell type–specific genetic and optogenetic tools reveal hippocampal CA2 circuits

Keigo Kohara[1,6], Michele Pignatelli[1,6], Alexander J Rivest[1,6], Hae-Yoon Jung[1], Takashi Kitamura[1], Junghyup Suh[1], Dominic Frank[1], Koichiro Kajikawa[1], Nathan Mise[2,5], Yuichi Obata[2], Ian R Wickersham[3] & Susumu Tonegawa[1,4]

The formation and recall of episodic memory requires precise information processing by the entorhinal-hippocampal network. For several decades, the trisynaptic circuit entorhinal cortex layer II (ECII)→dentate gyrus→CA3→CA1 and the monosynaptic circuit ECIII→CA1 have been considered the primary substrates of the network responsible for learning and memory. Circuits linked to another hippocampal region, CA2, have only recently come to light. Using highly cell type–specific transgenic mouse lines, optogenetics and patch-clamp recordings, we found that dentate gyrus cells, long believed to not project to CA2, send functional monosynaptic inputs to CA2 pyramidal cells through abundant longitudinal projections. CA2 innervated CA1 to complete an alternate trisynaptic circuit, but, unlike CA3, projected preferentially to the deep, rather than to the superficial, sublayer of CA1. Furthermore, contrary to existing knowledge, ECIII did not project to CA2. Our results allow a deeper understanding of the biology of learning and memory.

The hippocampus has a cardinal role in the acquisition and recall of episodic memory[1]. For several decades[2], the trisynaptic circuit ECII→dentate gyrus→CA3→CA1 has provided the anatomical substrate for memory circuit functions, such as pattern separation and pattern completion, as demonstrated by both modeling[3] and experimentation[4–7]. The hippocampus, however, includes an additional subregion, CA2 (ref. 8). The CA2 region is classically defined as the area located between the CA3 and the CA1 regions with large pyramidal cells that, in contrast with CA3 cells, lack thorny excrescences (complex spines) on the apical dendrites and lack innervation from the dentate gyrus[8,9]. An additional classical criterion for the CA2 region is strong hypothalamic afferents from the supramammillary nucleus (SUM)[9–11]. Recent electrophysiological studies have proposed that CA2 is the relay of a potent monosynaptic pathway, receiving strong afferents from both ECII and ECIII and innervating CA1 pyramidal cells[12,13]. In addition to the monosynaptic inputs provided by the perforant and temporoammonic paths, CA2 receives a direct input from CA3 (refs. 13,14). Synaptic transmissions at the ECIII-CA2 and ECII-CA2 connections are strong and highly plastic[13], whereas at the CA3-CA2 synapses connections are dominated by feedforward inhibition[13] and are resistant to long-term potentiation[14,15].

The CA2 region has been shown to expresses multiple region-specific genes[15–17], and a recent study using *in situ* hybridization proposed a redefinition of the CA2 region that is substantially wider than previously thought[18]. However, the relationship between the putative CA2 region newly proposed by molecular markers and the region classically defined by cellular and anatomical criteria remains unclear. Furthermore, the current knowledge about the afferents and efferents of CA2 is based on electrophysiological stimulation of axon bundles and/or dye injections into the source or target areas in which the specificity is potentially compromised. Defining this underexplored hippocampal region more extensively and establishing its connections more precisely are crucial for our understanding of the hippocampus, the brain system that has a pivotal role in episodic learning and memory[1].

Using cell type–specific methods of high resolution, we investigated the relationships between the new molecularly defined CA2 region and its classic anatomical criteria. We found a major unsuspected projection from dentate granule cells to CA2 pyramidal cells (dentate gyrus–CA2) that extended mainly along the longitudinal axis of the hippocampus. Contrary to previous reports[13,15–17,19], we observed that ECIII cells did not project directly to CA2 pyramidal cells in any substantial way. We explored the CA2 cell efferents and found a differential innervation of CA2 pyramidal cells to deep and superficial sublayers of CA1 pyramidal cells. These findings force a major revision of the projection pattern of the entorhinal-hippocampal network for episodic memory.

RESULTS
A new definition of CA2
The putative CA2 marker genes (RGS14 (ref. 20), PCP4 (ref. 18) and STEP[21]) were highly coexpressed in the putative CA2 pyramidal cells (PCP4 and RGS14 = 98% ± 1, STEP and RGS14 = 100%, PCP4 and

Figure 1 Molecular, cellular, anatomical and electrophysiological definition of the CA2 region of the hippocampus. (**a**–**d**) Representative images showing the expression of putative CA2 markers RGS14 (**a**), PCP4 (**b**) and STEP (**c**), as well as a superposed image (**d**). (**e**–**h**) Magnified confocal images of the boxed area in **d**. (**i**,**j**) z-axis-projected confocal images of RGS14-positive CA2 neurons (**i**) and dendritic spine morphologies of CA2 neurons visualized by DiI (**j**). Scale bar in **i** is the same as **j**. (**k**,**l**) Typical dendritic morphologies of CA2 neurons showing a lack of complex spines (**k**) and CA3 neurons with complex spines (**l**). Scale bar in **k** is the same as **l**. (**m**–**p**) The axonal dye tracer BDA was injected into the SUM. Injection site and diagram (bottom) showing axonal projections from SUM to CA2 and dentate gyrus (**m**). A z-axis-projected confocal image of BDA-positive terminals is shown in **n**. A magnified image of the boxed area in **n** is presented in **o**, showing overlay between PCP4 and BDA. A single confocal stack from the boxed area in **o** is presented in **p**, showing overlay between PCP4-expressing dendrites and BDA-positive terminals. (**q**) Representative z-projected confocal image of a biocytin-stained CA2 pyramidal cell. Right, single confocal stacks of the boxed region showing biocytin (top) and RGS14 staining (bottom). (**r**) Patch-clamp recording from a CA2 pyramidal cell (same as shown in **q**) in current-clamp configuration showing the response to a positive step current injection. Note the late firing preceded by a slow depolarizing ramp. Inset, magnification of an action potential showing the fast hyperpolarizing potential. (**s**) I-V curve; traces are from the cell shown in **q**. Double arrowhead indicates the slow depolarizing ramp. (**t**) I-V for n = 11 cells (mean ± s.e.m.), linear fit is shown in red.
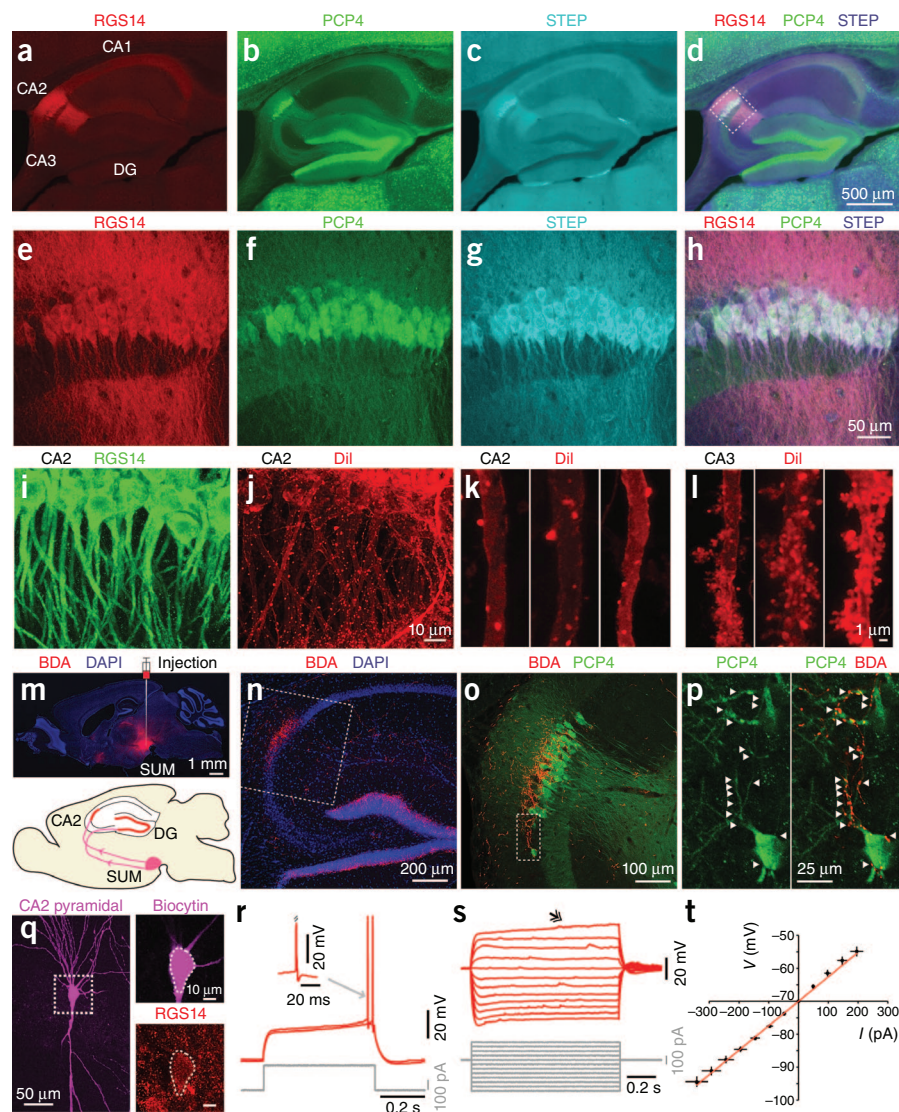
STEP = 98% ± 1, $n = 6$ mice; **Fig. 1a–h**). The expression of RGS14 did not overlap with that of the CA1 marker gene *Wfs1* (ref. 22), nor of a transgenic CA3 marker[4] (**Supplementary Fig. 1**). PCP4-positive CA2 cells did not express GAD67, but did express CaMKIIα, indicating that the cells had an excitatory nature (**Supplementary Fig. 2**). Furthermore, most of the PCP4-positive cells also expressed α-actinin2, a marker employed by another recent work[13] to help identify CA2 cells (**Supplementary Fig. 3**).

We visualized the dendrites of CA2 neurons with diolistic labeling and found that none of the RGS14-positive neurons had complex spines, instead only having simple spines in the stratum lucidum (43 of 43 RGS14-positive neurons without complex spines, $n = 4$ mice; **Fig. 1i–k**), consistent with the classical criterion for CA2 cells[9]. In contrast, most of the RGS14-negative CA3 neurons had complex spines on their dendrites (29 of 30 RGS14-negative neurons had complex spines, $n = 4$ mice; **Fig. 1l**) as reported previously[9,23]. We also injected an anterograde axonal tracer, biotinylated dextran amine (BDA) into SUM and examined the projection pattern from SUM to the hippocampus. We found that BDA-positive SUM projections overlapped with dentate gyrus granule cells (DGGCs), as shown previously[9–11], and with PCP4-positive CA2 cells ($n = 3$ mice; **Fig. 1m–p**), satisfying another classical criterion of CA2 cells[9–11].

The RGS14-positive putative CA2 pyramidal cells exhibited intrinsic electrophysiological properties, including a resting membrane potential of -70 ± 1 mV, input resistance of 78 ± 6 MΩ, membrane time constant of 27 ± 1 ms, action potential threshold of -44 ± 1 mV, sag amplitude

of 1 ± 0.2 mV and a persistent depolarization in response to somatic injection of positive current steps near the action potential threshold. These electrophysiological properties of RGS14-positive pyramidal cells were shared by the α-actinin2–positive CA2 cells[13] and distinguished them from RGS14-negative CA3 and CA1 pyramidal cells (**Fig. 1q–t** and **Supplementary Fig. 4**). There was no evidence of heterogeneity in these properties along the ~300-μm-wide band of RGS14-positive cells (**Supplementary Fig. 4**). Furthermore, CA2 cells defined by RGS14 seemed to have similar soma sizes (average soma surface 309 ± 30 μm²) and dendritic morphology as those defined by α-actinin2 (**Supplementary Fig. 4**)[13]. Thus, cells expressing the molecular markers for CA2 satisfy classical criteria with respect to both their dendritic spine morphology and projections from the SUM[8–11], as well as more recently reported criteria of their intrinsic electrophysiological properties[13].

Dentate mossy fibers innervate CA2 pyramidal cells

Using immunohistochemistry and viral tracing, we examined whether the newly defined CA2 pyramidal cells lacked mossy fiber innervation, another classical criterion of CA2 cells[8,9]. To our surprise, we found that calbindin-positive mossy fibers[24] projected extensively to PCP4-positive CA2 neurons in the stratum lucidum (the percentage of PCP4-positive cells overlapping with mossy fibers was 82.2 ± 1.1%, that of cells not

Figure 2 Dentate mossy fiber (MF) projections to CA2. (**a**) Confocal image showing PCP4 and calbindin staining in CA2. (**b**) Magnification (top) of the boxed region in **a** and quantification (bottom) of the numbers of PCP4-positive CA2 cells receiving calbindin-positive mossy fibers (MF+) or not receiving mossy fibers (MF–). Data are presented as mean ± s.e.m. Dotted line indicates mossy fiber ending point. (**c**) Confocal image showing ZnT3 and RGS14 staining in CA2. (**d**) Superposed image of ZnT3, VGluT1 and RGS14. Dotted lines in **c** and **d** enclose stratum lucidum. (**e**) Confocal image showing RGS14-positive dendrites in CA2. (**f**) Confocal image showing RGS14-positive dendrites and ZnT3-positive clusters. (**g**) Confocal image showing RGS14-positive dendrites and PSD95-positive clusters. (**h**) Superposed image showing ZnT3-PSD95 double-positive clusters on RGS14-positive dendrites. Bottom, magnification of boxed region showing ZnT3-positive, PSD95-positive, and ZnT3 and PSD95 double-positive clusters (arrowheads). (**i**) ChETA-YFP HSV construct (top). Confocal image of mossy fibers visualized by ChETA-YFP (bottom). (**j,k**) Z projection of the boxed region in **e** centered on CA3 (**j**) and CA2 (**k**). (**l**) Cumulative histogram of mossy fiber terminal diameters for CA2 ($n = 60$ boutons) and CA3 ($n = 43$ boutons). KS, Kolmogorov-Smirnov P value.
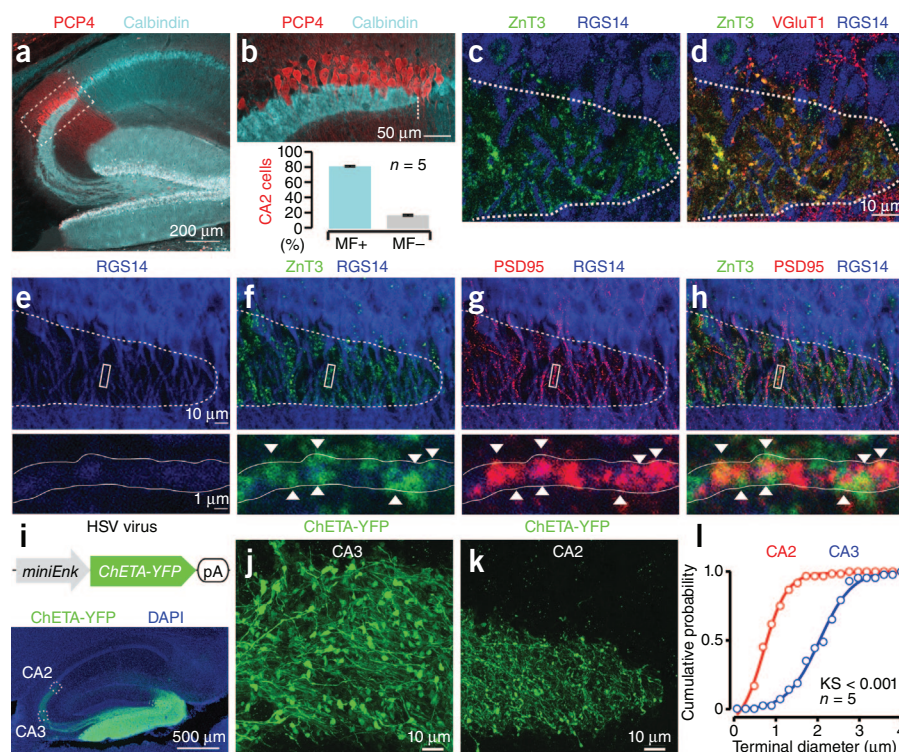
overlapping with mossy fibers was $17.8 \pm 1.1\%$, $n = 5$ mice; **Fig. 2a**,**b** and **Supplementary Figs. 5** and **6**). Next, we examined the distribution of ZnT3 (ref. 25), a presynaptic vesicle marker of mossy fibers, and VGluT1, a glutamatergic presynaptic vesicle marker, in the stratum lucidum of CA2. We found that ZnT3 and VGluT1 double-positive presynaptic clusters were located on RGS14-positive dendrites (**Fig. 2c**,**d**). Furthermore, we found that ZnT3 clusters overlapped with a postsynaptic marker, PSD95, on RGS14-positive dendrites (**Fig. 2e**–**h**). These data suggest that, contrary to the classical definition[8,9], mossy fibers form synaptic contacts with CA2 pyramidal neurons. We examined the morphology of mossy fiber terminals by infecting dentate gyrus with HSV mini-Enk promoter–ChETA–yellow fluorescent protein (YFP) (**Fig. 2i**) and found that CA2 received small mossy fiber boutons in contrast to the giant mossy fiber boutons received by CA3[9] (average bouton diameters: CA2, 0.97 ± 0.05 μm, $n = 60$ boutons; CA3, 2.11 ± 0.1 μm, $n = 43$ boutons; from $n = 5$ mice, Kolmogorov Smirnov $P < 0.001$; **Fig. 2j**–**l**).

The longitudinal component of mossy fibers projects into CA2
Mossy fibers are known to extend both transversally in a lamella and longitudinally in the septotemporal direction[26]. However, the longitudinal component has been thought to run exclusively in CA3 (refs. 9,26–28). To reinvestigate this issue, we visualized axonal projections from a limited population of DGGCs by injecting Cre-dependent tTA lentivirus and adeno-associated virus (AAV9-TRE-ArchT-GFP) into the dorsal dentate gyrus of a DGGC-specific Cre transgenic mouse (*Dock10-cre*; **Fig. 3a** and **Supplementary Fig. 7**). We found that, although mossy fibers projected mainly in the transverse plane in CA3, they abundantly projected longitudinally in CA2 up to ~2 mm (**Fig. 3b**–**e**).

To determine the extent and the direction of the longitudinal projection of mossy fibers in CA2, we applied the same approach, but infected only dorsal, intermediate or ventral dentate gyrus ($n = 3$ mice per group). Mossy fibers from dorsal DGGC extended to dorsal and intermediate CA2, but not to ventral CA2 (**Fig. 3f**,**i**,**l**,**o**), mossy fibers from intermediate DGGC extended to intermediate and ventral CA2,

but not to dorsal CA2 (**Fig. 3g**,**j**,**m**,**p**), and mossy fibers from ventral DGGC did not extend to dorsal or intermediate CA2 (**Fig. 3h**,**k**,**n**,**q**). These results indicate that the longitudinal component of mossy fibers projects exclusively in the septotemporal direction. Analysis of the mossy fiber terminal distribution confirmed that the septotemporal longitudinal component of mossy fibers mostly innervates the CA2 region, although a small fraction of the very distal CA3 region, adjacent to CA2, also received scattered innervations (percent of mossy fiber terminals: CA2 = 90%, CA3 = 10%, $n = 680$ mossy fiber terminals from 6 mice, two-tailed paired t test, $P < 0.05$).

DGGC–CA1 pyramidal cell monosynaptic connections
We then examined whether DGGCs and CA2 pyramidal cells are functionally connected. For this purpose, we infected DGGC-specific Cre transgenic mice with a Cre-dependent adeno-associated virus carrying channelrhodopsin2 (ChR2)-YFP[29] (AAV9-EF1α-DIO-ChR2-YFP) to allow DGGC-specific expression of ChR2-YFP (**Fig. 4a**–**c** and **Supplementary Fig. 7**). Optogenetic stimulation of ChR2-YFP–positive mossy fibers during patch-clamp recording from RGS14-positive CA2 pyramidal cells revealed a reliable excitatory synaptic current (average excitatory postsynaptic current (EPSC) amplitude = -122 ± 33 pA, $n = 23$; **Fig. 4d**–**f**). The EPSCs were sensitive to ionotropic glutamate receptor antagonists (10 μM NBQX, 100 μM AP5, $n = 5$) and to the antagonist of type II metabotropic glutamate receptors (1 μM DCG-IV, $n = 5$), a known blocker of mossy fiber synaptic transmission[13,30] (**Fig. 4g**). Bath application of GABA receptor antagonists did not abolish the synaptic response (10 μM GBZ, 2 μM CGP; average excitatory postsynaptic potential (EPSP) amplitude: control, 6 ± 1.9 mV; GBZ/CGP, 7.2 ± 2 mV; $n = 8$).

To test whether the dentate gyrus–CA2 connection was monosynaptic, we stimulated mossy fibers optogenetically and directly compared the onset of CA1, CA2 and CA3 pyramidal cell EPSCs in the same hippocampal slices. CA2 responses displayed a rapid onset comparable to those of CA3 responses, whereas CA1 responses displayed a delayed
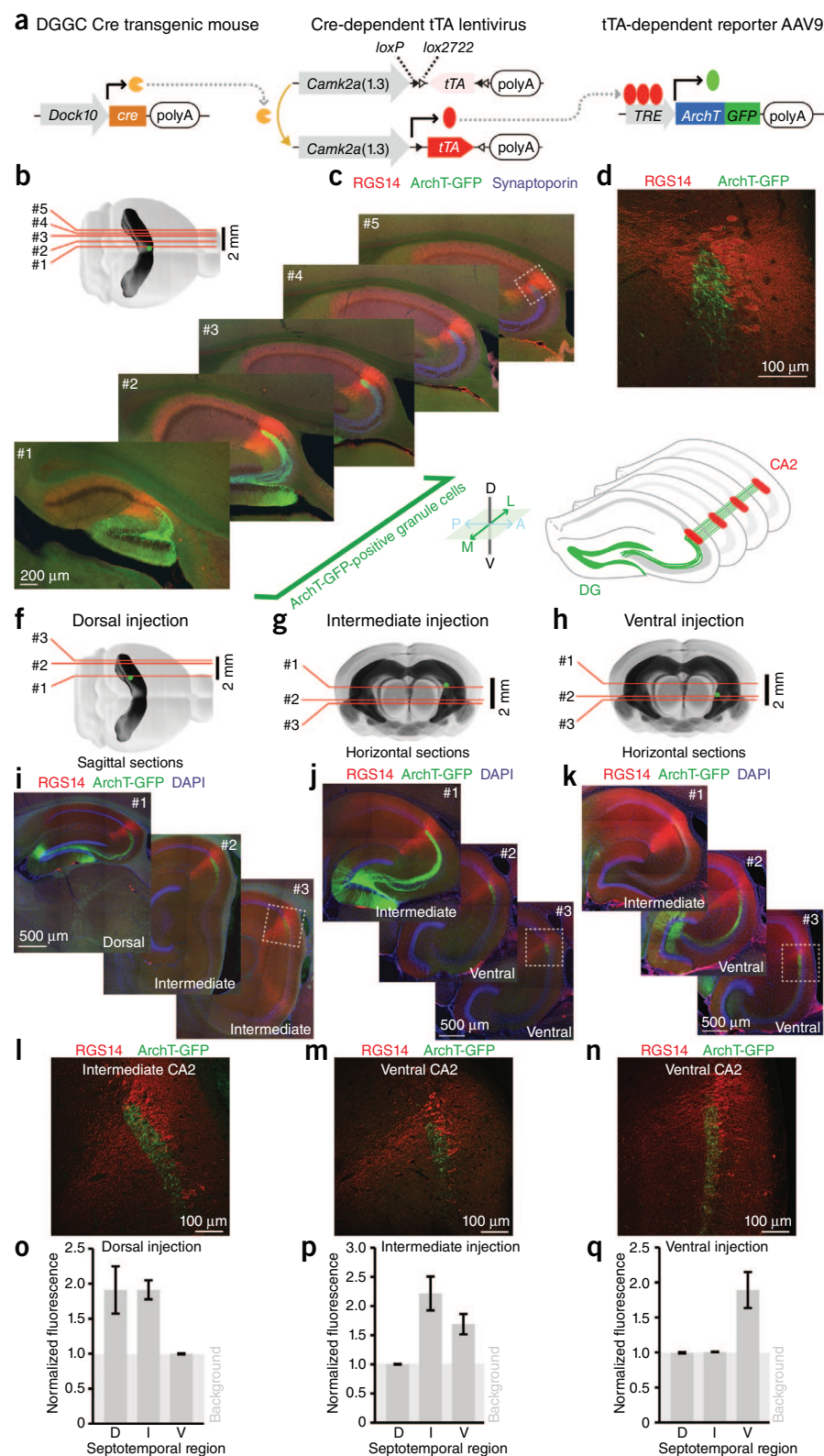
Figure 3 Longitudinal projections of dentate mossy fibers in CA2. (**a**) Schematic of DGGC-specific transgenic Cre mouse, Cre-dependent tTA lentivirus and tTA-dependent ArchT-GFP-AAV9. Cre recombinase switches on the expression of tTA in DGGCs, inducing the expression of ArchT-GFP. (**b**) Dorsorostral injection site (green) and location of serial sections shown in **c**. (**c**) Serial images of RGS14, ArchT-GFP and synaptoporin (mossy fiber marker). Dentate gyrus cells in sections 1–3 expressed ArchT-GFP. (**d**) Confocal image of the boxed region in **c**. (**e**) Longitudinal projections of mossy fibers in CA2. (**f**–**h**) The same approach was applied to dorsal (**f**), intermediate (**g**) and ventral (**h**) dentate gyrus injection sites (green dots). The locations of the serial sections shown in **i**–**k** are shown. (**i**–**k**) Images showing the extent and direction of mossy fibers (green) in the RGS14-positive (red) CA2 region for dorsal (**i**), intermediate (**j**) and ventral (**k**) dentate gyrus injection sites. (**l**–**n**) Magnified confocal images from the corresponding boxed regions shown in **i**, **j** and **k**. (**o**–**q**) Normalized fluorescence intesity of GFP-positive mossy fibers terminals in dorsal (D), intermediate (I) and ventral (V) CA2 for dorsal (**o**), intermediate (**p**) and ventral (**q**) dentate gyrus injection sites ($n = 6$ samples per group from $n = 3$ mice per injection site). Data are presented as mean ± s.e.m.

from CA3 cells (CA3 firing probability = 0.36 ± 0.04, $n = 20$ trials per cell; average action potential peak time = 3.85 ± 0.34 ms, $n = 14$ CA3 pyramidal cells; **Supplementary Fig. 8**). These results suggest a functional and direct excitatory monosynaptic connection from DGGCs to CA2 pyramidal cells and reinforce our anatomical observations (**Fig. 2**).

## Effect and modulation of the dentate gyrus–CA2 connection

Optogenetic stimulation of mossy fibers with a single light pulse combined with recordings of CA2 pyramidal cells in current mode revealed spiking activity in 22% of the cells (5 of 23). However, a 30-Hz train of 15 light pulses revealed spiking activity in 61% of the cells (14 of 23). Spike probability in response to the first pulse was 0.23 ± 0.1 (20 trials per cell, $n = 23$) and doubled during the next train pulses, with a spike probability of 0.43 ± 0.2 in response to a recovery pulse delivered 500 ms after the train (**Fig. 5a–d**). These results suggest dynamics ruled by synaptic facilitation. Analysis of the EPSP in response to single light pulse revealed a large EPSP (average EPSP amplitude = 4.7 ± 0.8 mV, $n = 24$) followed by inhibition (**Fig. 5e**). Inhibition was primarily sensitive to a GABAb receptor antagonist (2 μM CPG), and application of a GABAa antagonist (50 μM GBZ) induced a fast inhibitory response overlapping with the excitatory one (**Fig. 5f,g**). These results indicate the presence of feedforward inhibition elicited by mossy fiber activation. CA2 pyramidal cells are known to be locally controlled by CA2 interneurons[31], and the observed feedforward inhibition could be

onset that was accountable to polysynaptic connection (average EPSC onset: CA1, 7.04 ± 0.48 ms; CA2, 2.02 ± 0.13 ms; CA3, 1.58 ± 0.07 ms; $n = 9$ triplets; **Fig. 4h–j**). In addition, the onset of the CA2 response always preceded the occurrence of the first action potential peak elicited in CA3 cells through mossy fiber activation, excluding the possibility that CA2 EPSCs were mediated by a polysynaptic connection
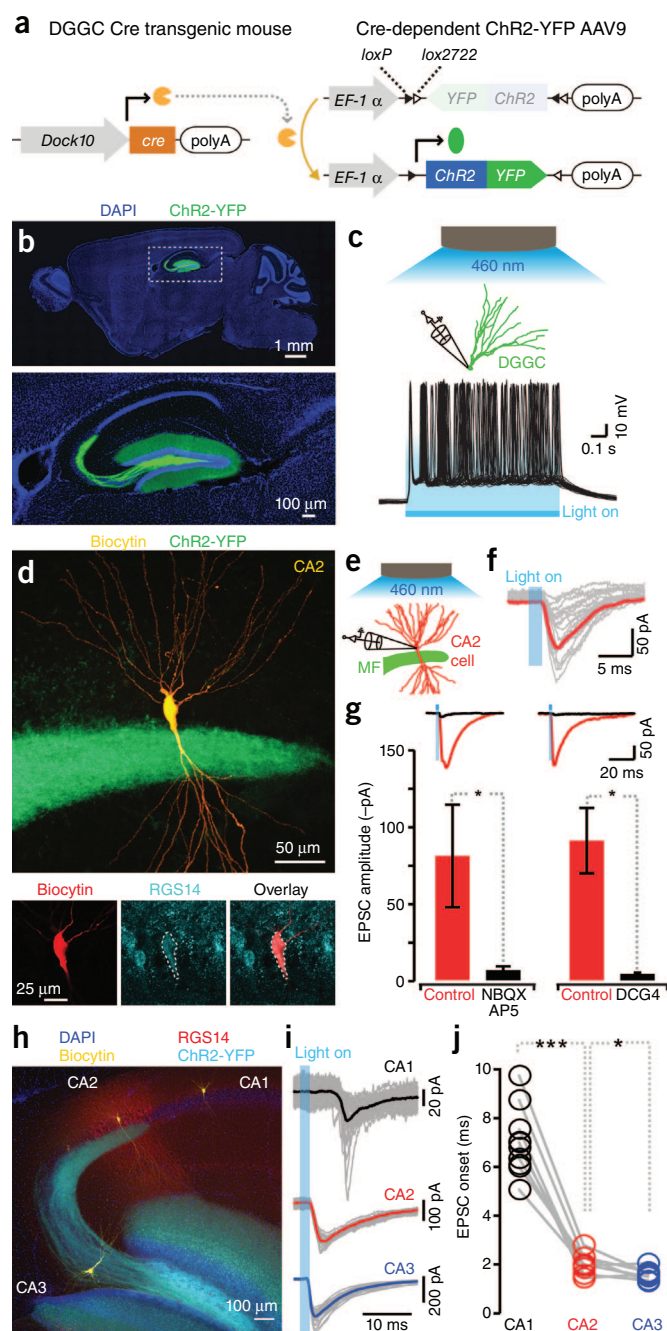
Figure 4 Functional monosynaptic connection of mossy fiber terminals onto CA2 pyramidal cells. (**a**) DGGC-specific Cre transgenic mice were injected with Cre-dependent AAV9-EF1α-ChR2-YFP. Cre recombinase switches on the expression of ChR2-YFP in DGGCs. (**b**) DGGC-specific expression of ChR2-YFP (top) and enlarged image from the boxed region (bottom). (**c**) Optogenetic stimulation of ChR2-YFP–positive DGGCs. (**d**) Zeta-projected confocal image of a recorded CA2 pyramidal cell (yellow) overlapped with ChR2-YFP–positive mossy fibers (green). Bottom, single confocal stacks showing colocalization of biocytin (red) and RGS14 (cyan). (**e**) Patch-clamp recording of CA2 pyramidal cell and optogenetic stimulation of mossy fibers in acute hippocampal slice. (**f,g**) Optogenetic stimulation of mossy fibers elicited an EPSC in a CA2 pyramidal cell (**f**), which was sensitive to NBQX and AP5 ($n = 5$, two-tailed paired t test, *$P < 0.05$) and DCG-IV ($n = 5$, two-tailed paired t test, *$P < 0.05$) (**g**). Data are presented as mean ± s.e.m. (**h**) Representative z-axis-projected confocal image of CA1, CA2 and CA3 pyramidal cells recorded in the same slice. (**i,j**) EPSCs recorded in CA1, CA2 and CA3 pyramidal cells elicited by optogenetic stimulation of mossy fibers (**i**). CA2 and CA3 cells displayed a fast EPSC onset, whereas CA1 cells displayed a delayed onset (**j**, $n = 9$ triplets; CA1 and CA2, two-tailed paired t test, ***$P < 0.001$; CA3 and CA2, *$P < 0.05$).

stratum oriens ($n = 2$), the deep stratum pyramidale ($n = 2$), or the border between lucidum and pyramidale ($n = 7$).

Our results demonstrate a functional monosynaptic connection between mossy fibers and CA2 interneurons and support the feed-forward inhibition observed in the CA2 pyramidal cells in response to optogenetic stimulation of mossy fibers. As reported for CA3 interneurons[32], local CA2 interneurons also receive direct projections from dentate gyrus, constituting a feedforward inhibitory mechanism that could control the output of CA2 pyramidal cells by modulating their rate or by controlling their timing.

Lack of direct projections from ECIII to the CA2 region

It has been reported that the CA2 region is the convergence point of direct cortico-hippocampal projections from ECII and ECIII[13]. However, the previous study did not employ an entirely cell or axon type–specific stimulation method. To selectively label MECIII axons with YFP, we injected AAV9-EF1α-DIO-ChR2-YFP virus into the entorhinal cortex of MECIII pyramidal cell–specific *Oxr1-cre* transgenic mice[33] (**Fig. 6a**). To selectively label MECII projections, we stained hippocampal slices of these mice for netrin-G2, a MECII-specific marker[34]. YFP-positive MECIII cell axons terminated sharply at the proximal end of the calbindin-positive CA1 region, and did not enter the RGS14-positive CA2 or extend to CA3 (**Fig. 6a** and **Supplementary Fig. 9**). Consistent with a prior report[35], netrin-G2–positive fibers extended beyond the dentate gyrus and terminated in the stratum lacunosum-molecular (SLM) of CA3 and CA2 (**Fig. 6a**). We considered the possibility that ChR2 might not be sufficiently expressed in some MECIII cells in the transgenic mice infected by the Cre-dependent AAV. We therefore injected a non–Cre-dependent and excitatory neuron–specific AAVrh8-CaMKIIα-ChR2-YFP virus into the entorhinal cortex superficial layers of wild-type mice. It is known that ECIII cells, but not ECII cells, innervate the contralateral hippocampus[36,37]. The contralateral component of ECIII axons did not enter the CA2 region of the wild-type mice (**Supplementary Fig. 10a–d**). Furthermore, when we investigated the cortico-hippocampal projections arising from the lateral entorhinal cortex (LEC), we found no overlap between LECIII fibers and the CA2 region, confirming previous findings[36,37] (**Supplementary Fig. 10e,f**).

Using MECIII cell type–specific optogenetic stimulation, we investigated the synaptic transmission of MECIII fibers to CA1, CA2 and CA3 pyramidal cells (**Fig. 6b**). Consistent with our anatomical observation, only CA1 cells displayed an excitatory response (average EPSC amplitude: CA1, −18 ± 3 pA, $n = 18$; CA2, 0 pA, $n = 10$; CA3, 0 pA, $n = 8$;

mediated by these interneurons. Indeed, optogenetic stimulation of mossy fibers with a single light pulse elicited spiking activity in 46% (5 of 11, average firing probability = 0.56 ± 18) of the CA2 interneurons recorded in current mode (**Fig. 5h,i**). Analysis of the first action potential peak time confirmed the possibility of a fast feedforward inhibitory circuit (average action potential peak time = 4.9 ± 0.6 ms; **Fig. 5j**). When recorded in voltage-clamp configuration, all CA2 interneurons responded to optogenetic stimulation of mossy fibers with a large EPSC (average EPSC amplitude = −138 ± 88 pA, average EPSC onset = 2.3 ± 0.1 ms, $n = 11$; **Fig. 5k**). We identified CA2 interneurons by biocytin staining, intrinsic electrophysiological properties and GAD67 expression ($n = 11$). Only a fraction of them expressed parvalbumin ($n = 3$), although both parvalbumin-positive and parvalbumin-negative CA2 interneurons displayed EPSCs in response to optogenetic stimulation of mossy fibers. The recorded CA2 interneurons were located in the
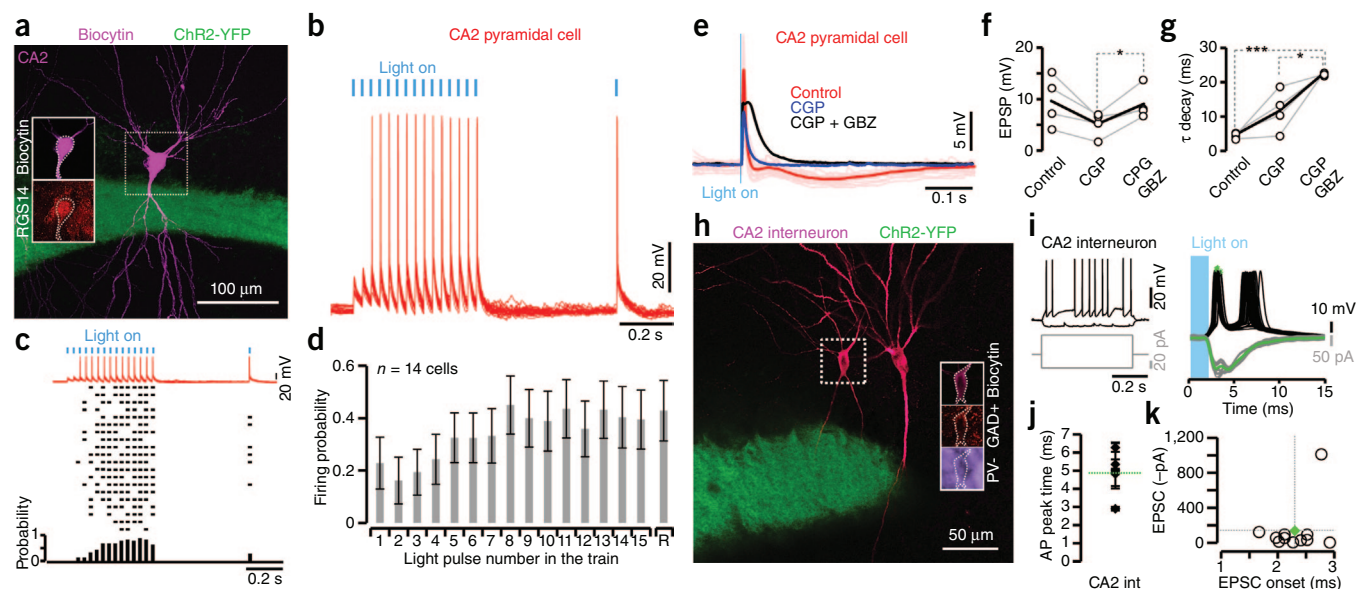
Figure 5 Response of CA2 cells to optogenetic stimulation of mossy fibers. (**a**) Z-projected confocal image of biocytin-filled CA2 pyramidal cell. Note the ChR2-YFP–positive mossy fibers. Inset, single confocal stacks of the boxed region showing biocytin (top) and RGS14 staining (bottom). (**b**) Patch-clamp recording from a CA2 pyramidal cell (same cell shown in **a**) in current mode showing the spiking activity in response to optogenetic stimulation (30-Hz train) of mossy fibers. (**c**) Spiking activity of the same CA2 cell. Bottom, firing probability. (**d**) Average firing probability in response to a 30-Hz train of light pulses for CA2 pyramidal cells ($n = 14$). Note the increased probability in the recovery pulse (R). Error bars represent mean ± s.e.m. (**e**) Current-clamp recording from a CA2 pyramidal cell in response to optogenetic stimulation of mossy fibers showing a large EPSP (average of 30 traces in red) followed by inhibition sensitive to antagonists of GABAergic transmission. (**f**,**g**) EPSP amplitude and decay, as shown in **e**, were affected by GABAa and GABAb antagonists (two-tailed paired t test, ***$P < 0.001$, *$P < 0.05$, $n = 4$). The average is indicted by the black lines. (**h**) Z-projected confocal image of a biocytin-filled (violet) CA2 interneuron. Inset, GAD67-positive and parvalbumin-negative CA2 interneuron from the boxed region. Note the ChR2-YFP–positive mossy fibers shown in green. (**i**) Current- (black) and voltage-clamp recordings (green) of the CA2 interneuron shown in **h** in response to optogenetic stimulation of mossy fibers. Note the spiking activity (action potential peak time is indicated by green asterisks). Inset, intrinsic electrophysiological properties in response to current steps. (**j**) First action potential peak times from CA2 interneurons ($n = 5$) in response to optogenetic stimulation of mossy fibers (average is indicated by the green dotted line). (**k**) EPSC amplitudes and onsets from CA2 interneurons ($n = 11$) in response to optogenetic stimulation of mossy fibers (average is indicated by the green dot).

average EPSC onset: CA1, 3.5 ± 0.2 ms, $n = 18$; **Fig. 6c,d**). CA1 EPSCs were sensitive to glutamate receptor antagonists (**Supplementary Fig. 11a–c**). Neither stronger train pulses (**Supplementary Fig. 11d–h**) nor stimulation after application of GABA receptor antagonists (**Supplementary Fig. 11i–o**) revealed a response in CA2. This observation was also confirmed by recording distal CA2 cells ($n = 5$) located
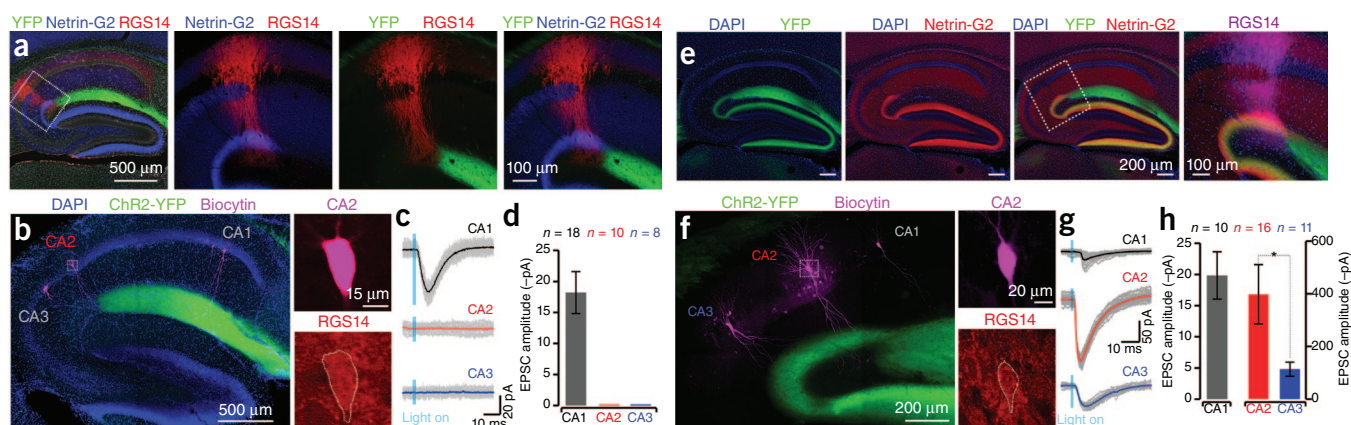
Figure 6 Cortico-hippocampal projections to CA2. (**a**) The entorhinal cortex of a MECIII-specific Cre mouse was injected with a Cre-dependent AAV9-EF1α-ChR2-YFP virus. Left, parasagittal hippocampal slice stained for RGS14, netrin-G2 (a MECII-specific marker) and DAPI (white). Right, enlarged confocal images of the boxed region. ChR2-YFP–positive MECIII fibers (green) were restricted to CA1-SLM and did not overlap with CA2. (**b**–**d**) Optogenetic stimulation of MECIII fibers. (**b**) Confocal image of biocytin-filled (violet) CA1, CA2 and CA3 pyramidal cells. Note the ChR2-YFP–positive MECIII fibers (green) in CA1-SLM. Right, CA2 pyramidal cell identified by colocalization of biocytin (violet) with RGS14 (red), magnified from the boxed region. (**c**) The same cells in voltage clamp in response to optogenetic stimulation of ChR2-YFP–positive MECIII fibers. (**d**) Only CA1 pyramidal cells displayed an excitatory response. (**e**) The entorhinal cortex of a wild-type mouse was injected with a non–Cre-dependent AAVrh8-CaMKIIα-ChR2-YFP virus. Shown is a parasagittal hippocampal slice expressing ChR2-YFP, stained for netrin-G2. Right, enlarged image from the boxed region. YFP-positive MECII fibers co-stained with netrin-G2 (yellow) running into the dentate gyrus and CA3 and overlapped with RGS14-positive dendrites of CA2. (**f**) Confocal image of biocytin-filled (violet) CA1, CA2 and CA3 pyramidal cells. Note the ChR2-YFP–positive (green) MECII/III fibers. Right, CA2 pyramidal cell identified by colocalization of biocytin (violet) with RGS14 (red). (**g**) Same cells in voltage clamp in response to optogenetic stimulation of ChR2-YFP–positive MECII/III fibers. (**h**) Average EPSC amplitudes for CA1, CA2 and CA3 pyramidal cells. Data are presented as mean ± s.e.m.

Figure 7 Mapping inputs to hippocampal CA2 neurons using the rabies virus–based monosynaptic tracing reveals MECII and LECII as the primary source of entorhinal inputs. (**a,b**) Schematic (**a**) and sagittal whole-brain section (**b**) from CA2-specific Cre mouse injected with helper AAV. Bottom, note the EGFP expression restricted to RGS14-positive CA2 pyramidal cells. (**c**) Sagittal whole-brain section from CA2-specific Cre mouse injected with helper AAV and rabies virus expressing AAV-specific EGFP signal (green), rabies virus–specific mCherry signal (red) and stained with Nissl (blue). (**d**) Percentage of cells expressing only mCherry in layers II and III of MEC (top) and LEC (bottom) ($n = 6$ samples from 3 mice, two-tailed paired t test, ***$P < 0.001$ and **$P < 0.005$, average in red). (**e,f**) Horizontal sections showing the cells expressing only mCherry in both MEC (**e**) and LEC (**f**). Dotted line indicates ECII/ECIII border.


in the pyramidal cell layer following the end of the stratum lucidum (**Supplementary Fig. 12**).

To analyze the ECII-mediated connectivity, we went back to the wild-type mice in which we injected a non–Cre-dependent and excitatory neuron–specific virus into the superficial layers of the entorhinal cortex (see above). In these mice, ChR2 was expressed in both MECIII and MECII (**Fig. 6e** and **Supplementary Fig. 13**). We then investigated the transmission at the synapses between MECII axons and CA2 or CA3 pyramidal cells (**Fig. 6f**). Given that MECIII projected exclusively to CA1 (**Fig. 6a,e** and **Supplementary Fig. 13**), any EPSCs recorded in CA2 or CA3 following optogenetic stimulation must be elicited by MECII axon activation. CA2 pyramidal cells displayed approximately fourfold larger EPSCs than CA3 cells, consistent with previous observations[13] (CA1, -20 ± 4 pA, $n = 10$; CA2, -403 ± 14 pA, $n = 16$; CA3, -115 ± 27 pA, $n = 11$; CA2 versus CA3, unpaired t test, $P < 0.05$; average EPSC onset: CA1, 3.3 ± 0.3 ms, $n = 10$; CA2 $2.5, \pm 0.1$ ms, $n = 16$; CA3, 2.8 ± 0.1 ms, $n = 11$; **Fig. 6f–h** and **Supplementary Fig. 11m–o**). Notably, EPSC amplitudes recorded in CA1 were comparable (two-tailed unpaired t test, $P = 0.75$) to those obtained in CA1 cells from *Oxr1-cre* mice injected with the Cre-dependent AAV9-EF1α-DIO-ChR2-YFP virus, consistent with the notion that MECII does not innervate CA1 (**Fig. 6h**).

Although it is unlikely[33], we could not exclude the possibility that axons from a small population of MECIII excitatory neurons were not labeled by YFP in the *Oxr1* transgenic mice. To exclude this possibility, we applied the rabies virus–based monosynaptic tracing technique[38] to CA2-specific Cre knock-in mice (*Map3k15-cre*; **Fig. 7a,b**). Contrary to the previously reported anatomical observations obtained with low cell type–specific retrograde tracers[19], entorhinal cortex cells presynaptic to CA2 pyramidal cells (labeled by mCherry) were detected mostly in MECII and LECII; there were very few cells present in MECIII or LECIII (**Fig. 7c–f** and **Supplementary Figs. 14** and **15**).

A new trisynaptic circuit: dentate gyrus–CA2-CA1$_{deep}$

Previous studies using classical anatomical criteria showed that CA2 projects to CA1 (refs. 8,9,21,39) and forms functional synaptic connections with CA1 pyramidal cells[13]. However, the manner in which the newly defined CA2 cells project to the downstream CA1 region remains unclear. We infected *Map3k15-cre* mice with a Cre-dependent virus, AAV9-EF1α-DIO-ChR2-YFP (**Fig. 8a–c** and **Supplementary Fig. 16**). All ChR2-YFP–positive cells expressed PCP4, confirming the high cell-type specificity of the knock-in mouse (PCP4 and YFP, 97% ± 0.4, $n = 3$ mice; **Supplementary Fig. 16**). Consistent with previous observations, CA2 axons traveled mainly into the stratum oriens (**Supplementary Fig. 16**)[8,21,39]. Optogenetic stimulation of ChR2-positive CA2 fibers during patch-clamp recordings from CA1 pyramidal cells revealed an excitatory response (average EPSC amplitude = -120 ± 20 pA, average EPSC onset = 1.9 ± 0.04 ms, $n = 28$) that was sensitive to ionotropic glutamate receptor antagonists (**Fig. 8d–g**).
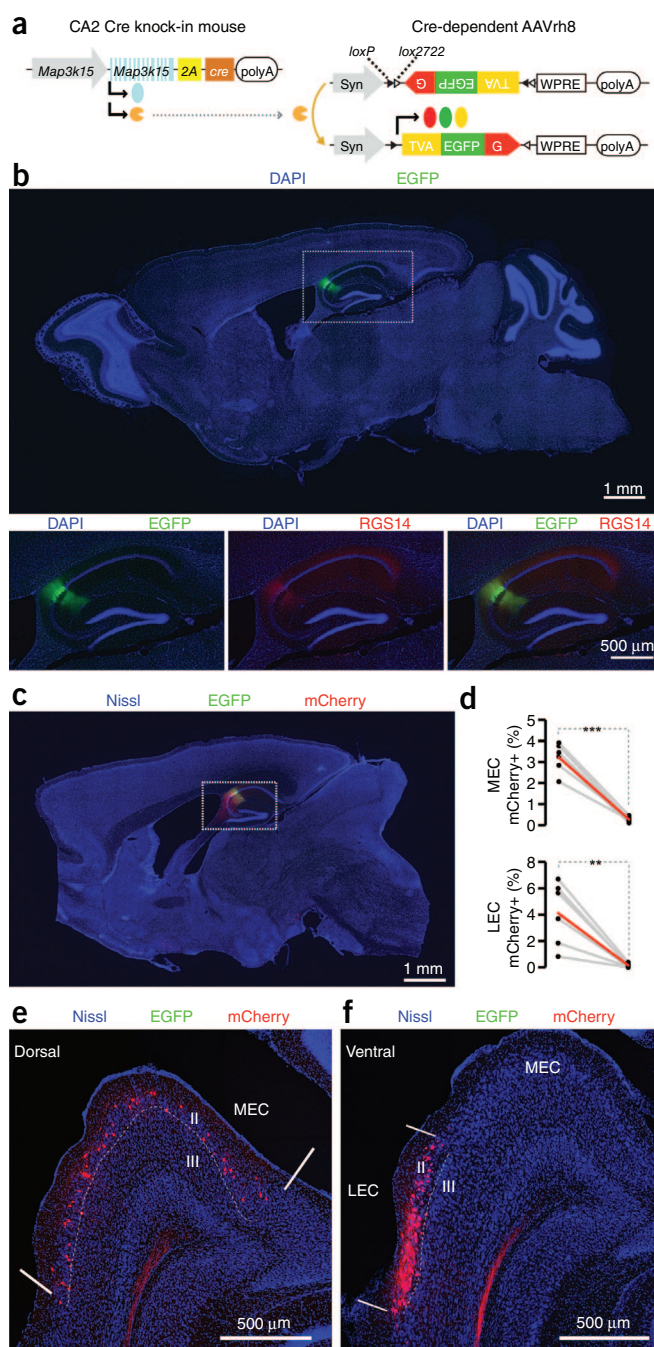
It was recently shown that the CA1 pyramidal cell layer consists of two sublayers, deep and superficial, which are distinct from each other by molecular markers[40] and by electrophysiological characteristics[41]. We compared the response of CA1 sublayer neurons in the same slices to CA2 stimulation and found that calbindin-negative deep CA1 pyramidal cells displayed an excitatory response stronger than that of calbindin-positive superficial CA1 cells (average EPSC amplitude: CA1$_{deep}$, -174 ± 33 pA; CA1$_{superficial}$, -63 ± 11 pA; $n = 14$ pairs, two-tailed paired t test, $P < 0.001$; average EPSC onset: CA1$_{deep}$, 1.8 ± 0.06 ms; CA1$_{superficial}$, 2 ± 0.05 ms; $n = 14$ pairs; **Fig. 8d–g,**). This result was not affected by blockers of GABAergic transmission, suggesting that the differential innervation of CA1$_{deep}$ and CA1$_{superficial}$ is mediated exclusively by excitatory synaptic connections (average EPSC amplitude after GBZ and CPG treatment: CA1$_{deep}$, -85 ± 18 pA, CA1$_{superficial}$,-41 ± 14 pA;
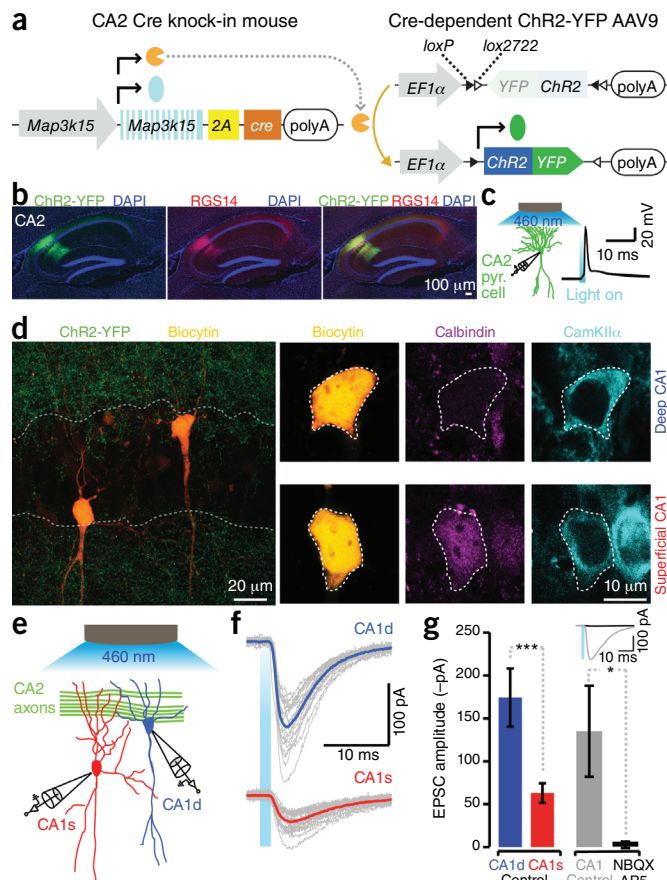
Figure 8 A preferential connection from CA2 to deep CA1 pyramidal cells establishes a previously unknown trisynaptic circuit, dentate gyrus–CA2-CA1$_{deep}$. (**a**) CA2-specific Cre knock-in mice were injected with Cre-dependent AAV9-EF1α-ChR2-YFP. Cre recombinase switches on the expression of ChR2-YFP in CA2. (**b**) ChR2-YFP expression in RGS14-positive CA2 cells. (**c**) Optogenetic stimulation of a ChR2-YFP–positive CA2 pyramidal cell. (**d**) Representative image of a recorded CA1 pyramidal cell pair located in different sublayers (dotted line indicates pyramidal cell layer). Top right, deep cells expressing CaMKIIα, but not calbindin. Bottom right, superficial cells expressing CaMKIIα and calbindin. (**e**) Patch-clamp recordings of CA1 superficial (CA1s) and deep (CA1d) pyramidal cells combined with optogenetic stimulation of CA2 fibers in acute hippocampal slices. (**f**,**g**) Optogenetic stimulation of CA2 fibers elicited EPSCs in a CA1 pyramidal cell pair. Deep pyramidal cells displayed a stronger response ($n = 14$ pairs, two-tailed paired t test, ***$P < 0.001$). EPSCs were sensitive to NBQX and AP5 ($n = 7$, two-tailed paired t test, *$P < 0.05$). Data are presented as mean ± s.e.m.

We found that the expression of additional molecular markers, RGS14, STEP and MAP3K15, overlapped with PCP4 expression almost perfectly. These molecularly defined pyramidal cells satisfied several classical criteria of CA2 cells: the lack of complex spines, presence of strong SUM afferents and relatively large soma sizes. Furthermore, the putative CA2 pyramidal cells defined by multiple molecular markers were distinguished from CA3 and CA1 pyramidal cells by several intrinsic electrophysiological properties that have recently been reported[13]. We found no major evidence of heterogeneity along the ~300-μm stretch of the RGS14-positive cells with respect to either spine morphologies (**Fig. 1i–k**) in the stratum lucidum or intrinsic electrophysiological properties (**Fig. 1q–t** and **Supplementary Fig. 4**).

The major deviations of the newly defined CA2 region from the classically defined one are direct innervation by mossy fibers and the greater width along the proxi-distal axis in the CA arc. We believe that these differences were revealed by our use of tools and technologies that permit higher levels of cell type–specific analysis at both presynaptic and postsynaptic sides and that were not available when the CA2 region was classically defined. We believe that the new definition of CA2 is more useful for future studies because the newly defined cells share common molecular, cellular, physiological and anatomical properties that distinguish them from the cells in the adjacent CA3 and CA1 regions.

A trisynaptic circuit, ECII→dentate gyrus→CA2→CA1$_{deep}$

CA2 was innervated by small mossy fiber boutons contacting the shaft and simple spines of the apical dendrites (**Fig. 2** and **Supplementary Fig. 18**). On the other hand, CA3 receives mossy fiber innervation on both the apical and basal dendrites, where giant boutons form synapses with the complex spines of CA3 neurons[9]. This distinction is illustrated by the greater response amplitude displayed by CA3 neurons following mossy fiber stimulation (average EPSC amplitude: CA2, −66 ± 19 pA; CA3, −939 ± 217 pA; $n = 9$ pairs recorded in the same slices, two-tailed paired t test, $P < 0.005$). However, the synapses formed by giant boutons and complex spines represent a unique case in the CNS, with an unusual synaptic transmission strength[42]. On dendrites, proximal synapses generally have a greater effect on neuronal activity than distal synapses[9]. Indeed, using optogenetic stimulation of the Schaffer collaterals in CA3-specific Cre transgenic mice, we found that the dentate gyrus–CA2 connection was stronger than the CA3-CA2 connection located on a more distal part of the apical dendrite (average EPSC amplitude: dentate gyrus–CA2, −122 ± 33 pA, $n = 23$; CA3-CA2, −40 ± 33 pA; $n = 10$, two-tailed unpaired t test, $P < 0.05$; **Supplementary Fig. 19**). Furthermore, the dentate gyrus–CA2 connection was stronger than some of the other connections in the cortico-hippocampal network, including ECIII to CA1 (ref. 13) and young granule cells to CA3 (ref. 30), two connections

$n = 7$, two-tailed paired t test, $P < 0.05$. In a CA3-specific Cre mouse[4], we found that, unlike CA2, CA3 innervated the two CA1 sublayers with equal strength (average EPSC amplitude: CA1$_{deep}$, −50 ± 17 pA; CA1$_{superficial}$, −42 ± 24 pA; $n = 7$ pairs, two-tailed paired t test, $P = 0.62$; average EPSC onset: CA1$_{deep}$, 3.6 ± 0.25 ms; CA1$_{superficial}$, 4.4 ± 0.8 ms; $n = 7$ pairs; **Supplementary Fig. 17**). Thus, we have identified a previously unknown trisynaptic circuit, dentate gyrus–CA2-CA1$_{deep}$, which runs parallel to the classical trisynaptic circuit dentate gyrus–CA3-CA1.

DISCUSSION

We combined several cell type–specific tools and technologies to examine hippocampal CA2 excitatory neurons and their circuits. Contrary to the traditionally held view, CA2 pyramidal cells received direct input from DGGCs, CA2 pyramidal cells did not receive direct input from ECIII cells and CA2 pyramidal cells projected preferentially to CA1 pyramidal cells in the deep sublayer.

The new definition of the CA2 region

The classical definition distinguishes CA2 pyramidal cells from CA3 pyramidal cells by a lack of complex spines on the apical dendrites[8], a lack of direct innervations of mossy fibers[8], and strong hypothalamic afferents from the SUM[10,11]. CA2 pyramidal cells have also been distinguished from CA1 pyramidal cells by their distinctly larger soma sizes and SUM afferents[8,11]. More recently, the putative CA2 cells were redefined by the molecular marker PCP4 (ref. 18). However, the extent to which these cells satisfy the classical morphological and anatomical criteria have not been rigorously investigated. Indeed, the molecularly defined CA2 region extends into a substantially wider area (~300 μm) than the classically defined one (~100 μm)[18] (**Supplementary Fig. 5**).

that are known for their effect on behavior[7,33]. Thus, it is likely that the newly found dentate gyrus–CA2 connection will also have a substantial effect on behavior, although it is currently only a matter of speculation as to the specific function of these connections.

One notable finding about the dentate gyrus–CA2 connections concerns the extensive longitudinal transfer of information along the septotemporal axis of the hippocampus. Previous studies have shown that mossy fibers consist of both transverse and longitudinal projections, with the latter running exclusively along the septotemporal direction[26,27]. Because CA2 has, by definition, been excluded from the targets of mossy fibers, the CA3 region, particularly the distal part known as CA3a[28], has been considered to be the exclusive target of these longitudinal projections. With the new definition of the CA2 region, we found that mossy fibers enter the CA2 region and proceed septotemporally in this region for a long distance (~2 mm; **Fig. 3**). Although 90% of the axonal boutons belonging to the longitudinal component were detected in the stratum lucidum of the CA2 region, only 10% could be detected in the CA3a region, adjacent to CA2. In addition, it has been reported that CA2 axons run septotemporally in the downstream CA1 region[21,39]. Thus, CA2 cells appear to be at the center of a septotemporal circuit covering the whole longitudinal axis of the hippocampus. Through the extensive longitudinal projections of mossy fibers and CA2 axons, the trisynaptic circuit that we describe could provide a substrate for a hierarchical association of information across hippocampal lamellae as compared with the classical trisynaptic circuit, which operates mainly with transverse projections[9]. For example, activation of dorsal dentate gyrus could easily recruit intermediate CA2 cells, which could have a direct effect on a more ventral CA1 cells, thereby establishing a direct link between dorsal and ventral hippocampus and providing a fast route to directly influence downstream regions connected to ventral CA1, such as prefrontal cortex and basolateral amygadala[43].

The CA2-linked trisynaptic circuit ECII→dentate gyrus→CA2→CA1 also differs from the classical one in the innervation of CA1. A previous study reported that the functional innervation of CA1 cells provided by CA2 cells is stronger than the one provided by CA3 cells[13]. However, this study did not distinguish between the deep and superficial sublayers of CA1 (ref. 40). CA2 axons are known to run preferentially in the stratum oriens[8,21,39], where both the extent of arborization of the basal dendrites and the spine numbers are greater for deep rather than superficial CA1 cells[44,45]. Consistent with the projection pattern of CA2 axons and with the dendritic morphology of CA1 cells, we found that the functional synaptic connections made by CA2 cells were about 2.5-fold stronger with the deep rather than superficial CA1 cells (**Fig. 8**). In contrast, Schaffer collaterals of CA3 cells functionally innervated the apical dendrites of both CA1 sublayers with equal strength (**Supplementary Fig. 17**). The CA2-linked trisynaptic circuit can exert a powerful downstream effect *in vivo* through the higher firing and bursting rates of the deep layer CA1 pyramidal cells[41]. Although the target of the CA1 sublayers remains unknown, it is possible that the information conveyed by the two trisynaptic circuits is directed to differential targets and thereby used for distinct functions.

Notably, the two trisynaptic circuits are not entirely independent, as they interact mutually between CA3 and CA2. The CA3-CA2 connections[46] are known to be dominated by feedforward inhibition[13]. Combining optogenetic stimulation of ChR2-YFP-positive CA2 fibers and patch-clamp recordings from CA3 pyramidal cells, we found that CA2-CA3 connections were also dominated by inhibition (**Supplementary Fig. 19**). This mutually inhibitory loop of the connections between CA2 and CA3 suggests a competitive relationship between the two trisynaptic circuits.

CA2 pyramidal cells lack direct input from ECIII

We have shown this by three methods, all with high cell-type specificity. First, YFP-labeled axons from MECIII-specific transgenic Cre mice did not overlap with RGS14-positive CA2 cells (**Fig. 6**). Second, MECIII cell–specific optogenetic stimulation (**Fig. 6**), even with a train of light pulses (**Supplementary Figs. 11** and **12**) or in the presence of GABA receptor antagonists (**Supplementary Fig. 11**), did not reveal any response in CA2 cells (**Supplementary Figs. 11** and **12**). Third, the rabies virus–based monosynaptic tracing technique conducted with CA2 pyramidal cell–specific Cre knock-in mice revealed only a few positive cells in MECIII or LECIII that may project to CA2 pyramidal cells (**Fig. 7**).

We did consider the possibility that the *Oxr1* promoter used for the generation of MECIII-specific transgenic mice is not active in some MECIII cells and that axons of these cells may reach the CA2 region and activate their pyramidal cells. However, the lack of any detectable overlap between contralateral ECIII cell axons and RGS14-positive cells in wild-type mice makes this possibility highly unlikely (**Supplementary Fig. 10**). These data are at odds with those of the previous study[13], which found that CA2 cells responded robustly to electric stimulation of axons in SLM. It is highly unlikely that electric stimulation of axons from the very few MECIII or LECIII cells observed by our rabies virus–based retrograde tracing experiment (**Fig. 7**) could account for the robust synaptic transmission and plasticity detected by the prior study[13]. In fact, these few MECIII and LECIII cells may actually be long-range inhibitory neurons, which are known to project to the hippocampus[47].

Could it be possible that both we and the prior study[13] recorded from two different sets of cells? The previous study[13] recorded from α-actinin2–positive large pyramidal cells "located in the area following the end of the mossy fiber tract" (**Supplementary Fig. 4** and ref. 14). In this area, virtually all α-actinin2–positive cells also expressed PCP4 (**Supplementary Fig. 3**). These PCP4-positive cells had the physiological properties characteristic of CA2 cells seen in the rest of the PCP4-positive cells (**Supplementary Fig. 4**). However, we failed to induce EPSCs from these distal CA2 cells, even with strong optogenetic stimulation of ChR2-positive axons of MECIII cells (**Supplementary Fig. 12**). In addition, recordings of very proximal CA1 pyramidal cells in response to optogenetic stimulation of MECIII fibers revealed only weak responses, typical of more distal CA1 cells (**Supplementary Fig. 11**). Despite all of these data and reasoning, one cannot exclude the possibility that the previous study[13] recorded from a subpopulation of cells, which we did not cover in our CA2 recording experiments.

Could it be possible that the axons stimulated by the two studies are not entirely the same? Unlike our approach, which used cell type–specific genetics, the prior study[13] employed electric stimulation of axonal bundles in the temporo-ammonic pathway. It is possible that fibers other than those from MECIII could also have been recruited[9]. It is even possible that the electricity spilled out to nearby ECII cell fibers (within ~60 μm), which run through the distal molecular layer of the dentate gyrus and are known to be a robust source of stimulation for CA2 pyramidal cells[13] (**Fig. 6**). The latter possibility (that is, electricity spillage) is suggested by the previous study's[13] observation that CA3a cells also responded substantially to the same stimulation of axon bundles in the temporo-ammonic pathway. These connections were also reported in earlier studies conducted with similar methods[48,49]. However, our cell type–specific axonal tracing and optogenetic stimulation experiments revealed that ECIII cells did not innervate CA3 cells (**Fig. 6**), suggesting that there may have been electricity spillage in the prior study's experiment[13]. Nevertheless, it is difficult to be certain that the conflicting results obtained stem from activation of different sets of axons.

In contrast with the lack of a CA2 response to ECIII axon stimulations, we confirmed the prior study's finding[13] that CA2 pyramidal

cells respond robustly to the stimulation of axons from ECII stellate cells (**Fig. 6f–h**). What emerge from these data are two mutually exclusive direct hippocampal projection patterns, ECIII→CA1 and ECII→dentate gyrus/CA3/CA2.

Potential implications

The classical trisynaptic circuit has been a fertile ground to which genetic manipulations targeted to specific subregions, and connections thereof have been applied to investigate their casual roles in specific aspects of entorhinal-hippocampal learning and memory, such as pattern separation and pattern completion[4–7]. In contrast, studies relevant to the role of the trisynaptic circuit linked to CA2 have only recently begun by knocking out genes richly expressed in CA2 (ref. 20). One suspected function of this circuit is to regulate overlearning by the classical trisynaptic circuit[15,20]. In this hypothetical regulation, the mutually inhibitory CA3→CA2 and CA2→CA3 connections at which the two trisynaptic circuits intersect may have a crucial role. On the other hand, the direct ECIII input dedicated to CA1 has been implicated in temporal association memory[33], and this input may also underlie encoding of the temporal order of events in an episode[50]. The cell type–specific Cre transgenic mice and optogenetics that we used promise to be highly useful for testing these and other hypotheses at the behavioral level.

METHODS

Methods and any associated references are available in the online version of the paper.

Note: Any Supplementary Information and Source Data files are available in the online version of the paper.

1. Bird, C.M. & Burgess, N. The hippocampus and memory: insights from spatial processing. *Nat. Rev. Neurosci.* **9**, 182–194 (2008).
2. Cajal, S.R.y. *Histology of the Nervous System of Man and Vertebrates* (Oxford University Press, 1995).
3. Marr, D. Simple memory: a theory for archicortex. *Philos. Trans. R. Soc. Lond. B Biol. Sci.* **262**, 23–81 (1971).
4. Nakazawa, K. *et al.* Requirement for hippocampal CA3 NMDA receptors in associative memory recall. *Science* **297**, 211–218 (2002).
5. McHugh, T.J. *et al.* Dentate gyrus NMDA receptors mediate rapid pattern separation in the hippocampal network. *Science* **317**, 94–99 (2007).
6. Nakashiba, T., Young, J.Z., McHugh, T.J., Buhl, D.L. & Tonegawa, S. Transgenic inhibition of synaptic transmission reveals role of CA3 output in hippocampal learning. *Science* **319**, 1260–1264 (2008).
7. Nakashiba, T. *et al.* Young dentate granule cells mediate pattern separation, whereas old granule cells facilitate pattern completion. *Cell* **149**, 188–201 (2012).
8. de Nó, R.L. Studies on the structure of the cerebral cortex. II. Continuation of the study of the ammonic system. *J. Psychol. Neurol. (Lpz)* **46**, 113–177 (1934).
9. Andersen, P. *The Hippocampus Book* (Oxford University Press, 2007).
10. Haglund, L., Swanson, L.W. & Köhler, C. The projection of the supramammillary nucleus to the hippocampal formation: an immunohistochemical and anterograde transport study with the lectin PHA-L in the rat. *J. Comp. Neurol.* **229**, 171–185 (1984).
11. Maglóczky, Z., Acsády, L. & Freund, T.F. Principal cells are the postsynaptic targets of supramammillary afferents in the hippocampus of the rat. *Hippocampus* **4**, 322–334 (1994).
12. Bartesaghi, R. & Gessi, T. Parallel activation of field CA2 and dentate gyrus by synaptically elicited perforant path volleys. *Hippocampus* **14**, 948–963 (2004).
13. Chevaleyre, V. & Siegelbaum, S.A. Strong CA2 pyramidal neuron synapses define a powerful disynaptic cortico-hippocampal loop. *Neuron* **66**, 560–572 (2010).
14. Zhao, M., Choi, Y.-S., Obrietan, K. & Dudek, S.M. Synaptic plasticity (and the lack thereof) in hippocampal CA2 neurons. *J. Neurosci.* **27**, 12025–12032 (2007).
15. Caruana, D.A., Alexander, G.M. & Dudek, S.M. New insights into the regulation of synaptic plasticity from an unexpected place: Hippocampal area CA2. *Learn. Mem.* **19**, 391–400 (2012).
16. Piskorowski, R.A. & Chevaleyre, V. Synaptic integration by different dendritic compartments of hippocampal CA1 and CA2 pyramidal neurons. *Cell. Mol. Life Sci.* **69**, 75–88 (2012).
17. Jones, M.W. & McHugh, T.J. Updating hippocampal representations: CA2 joins the circuit. *Trends Neurosci.* **34**, 526–535 (2011).
18. Lein, E.S., Callaway, E.M., Albright, T.D. & Gage, F.H. Redefining the boundaries of the hippocampal CA2 subfield in the mouse using gene expression and 3-dimensional reconstruction. *J. Comp. Neurol.* **485**, 1–10 (2005).
19. Cui, Z., Gerfen, C.R. & Young, W.S. Hypothalamic and other connections with the dorsal CA2 area of the mouse hippocampus. *J. Comp. Neurol.* **521**, 1844–1866 (2013).
20. Lee, S.E. *et al.* RGS14 is a natural suppressor of both synaptic plasticity in CA2 neurons and hippocampal-based learning and memory. *Proc. Natl. Acad. Sci. USA* **107**, 16994–16998 (2010).
21. Shinohara, Y. *et al.* Hippocampal CA3 and CA2 have distinct bilateral innervation patterns to CA1 in rodents. *Eur. J. Neurosci.* **35**, 702–710 (2012).
22. Lein, E.S. *et al.* Genome-wide atlas of gene expression in the adult mouse brain. *Nature* **445**, 168–176 (2007).
23. Gonzales, R.B., DeLeon Galvan, C.J., Rangel, Y.M. & Claiborne, B.J. Distribution of thorny excrescences on CA3 pyramidal neurons in the rat hippocampus. *J. Comp. Neurol.* **430**, 357–368 (2001).
24. Lein, E.S., Zhao, X. & Gage, F.H. Defining a molecular atlas of the hippocampus using DNA microarrays and high-throughput *in situ* hybridization. *J. Neurosci.* **24**, 3879–3889 (2004).
25. Wenzel, H.J., Cole, T.B., Born, D.E., Schwartzkroin, P.A. & Palmiter, R.D. Ultrastructural localization of zinc transporter-3 (ZnT-3) to synaptic vesicle membranes within mossy fiber boutons in the hippocampus of mouse and monkey. *Proc. Natl. Acad. Sci. USA* **94**, 12676–12681 (1997).
26. Swanson, L.W., Wyss, J.M. & Cowan, W.M. An autoradiographic study of the organization of intrahippocampal association pathways in the rat. *J. Comp. Neurol.* **181**, 681–715 (1978).
27. Amaral, D.G. & Witter, M.P. The three-dimensional organization of the hippocampal formation: a review of anatomical data. *Neuroscience* **31**, 571–591 (1989).
28. Sun, G.J. *et al.* Seamless reconstruction of intact adult-born neurons by serial end-block imaging reveals complex axonal guidance and development in the adult hippocampus. *J. Neurosci.* **33**, 11400–11411 (2013).
29. Zhang, F., Wang, L.-P., Boyden, E.S. & Deisseroth, K. Channelrhodopsin-2 and optical control of excitable cells. *Nat. Methods* **3**, 785–792 (2006).
30. Toni, N. *et al.* Neurons born in the adult dentate gyrus form functional synapses with target cells. *Nat. Neurosci.* **11**, 901–907 (2008).
31. Mercer, A., Trigg, H.L. & Thomson, A.M. Characterization of neurons in the CA2 subfield of the adult rat hippocampus. *J. Neurosci.* **27**, 7329–7338 (2007).
32. Acsády, L., Kamondi, A., Sik, A., Freund, T. & Buzsaki, G. GABAergic cells are the major postsynaptic targets of mossy fibers in the rat hippocampus. *J. Neurosci.* **18**, 3386–3403 (1998).
33. Suh, J., Rivest, A.J., Nakashiba, T., Tominaga, T. & Tonegawa, S. Entorhinal cortex layer III input to the hippocampus is crucial for temporal association memory. *Science* **334**, 1415–1420 (2011).
34. Nishimura-Akiyoshi, S., Niimi, K., Nakashiba, T. & Itohara, S. Axonal netrin-Gs transneuronally determine lamina-specific subdendritic segments. *Proc. Natl. Acad. Sci. USA* **104**, 14801–14806 (2007).
35. Tamamaki, N. & Nojyo, Y. Projection of the entorhinal layer II neurons in the rat as revealed by intracellular pressure-injection of neurobiotin. *Hippocampus* **3**, 471–480 (1993).
36. Steward, O. & Scoville, S.A. Cells of origin of entorhinal cortical afferents to the hippocampus and fascia dentata of the rat. *J. Comp. Neurol.* **169**, 347–370 (1976).
37. Steward, O. Topographic organization of the projections from the entorhinal area to the hippocampal formation of the rat. *J. Comp. Neurol.* **167**, 285–314 (1976).

38. Wickersham, I.R. *et al.* Monosynaptic restriction of transsynaptic tracing from single, genetically targeted neurons. *Neuron* **53**, 639–647 (2007).
39. Tamamaki, N., Abe, K. & Nojyo, Y. Three-dimensional analysis of the whole axonal arbors originating from single CA2 pyramidal neurons in the rat hippocampus with the aid of a computer graphic technique. *Brain Res.* **452**, 255–272 (1988).
40. Dong, H.-W., Swanson, L.W., Chen, L., Fanselow, M.S. & Toga, A.W. Genomic-anatomic evidence for distinct functional domains in hippocampal field CA1. *Proc. Natl. Acad. Sci. USA* **106**, 11794–11799 (2009).
41. Mizuseki, K., Diba, K., Pastalkova, E. & Buzsáki, G. Hippocampal CA1 pyramidal cells form functionally distinct sublayers. *Nat. Neurosci.* **14**, 1174–1181 (2011).
42. Rollenhagen, A. & Lübke, J.H.R. The mossy fiber bouton: the "common" or the "unique" synapse? *Front. Synaptic Neurosci.* **2**, 2 (2010).
43. Cenquizca, L.A. & Swanson, L.W. Spatial organization of direct hippocampal field CA1 axonal projections to the rest of the cerebral cortex. *Brain Res. Rev.* **56**, 1–26 (2007).
44. Bannister, N.J. & Larkman, A.U. Dendritic morphology of CA1 pyramidal neurones from the rat hippocampus. I. Branching patterns. *J. Comp. Neurol.* **360**, 150–160 (1995).
45. Bannister, N.J. & Larkman, A.U. Dendritic morphology of CA1 pyramidal neurones from the rat hippocampus. II. Spine distributions. *J. Comp. Neurol.* **360**, 161–171 (1995).
46. Ishizuka, N., Cowan, W.M. & Amaral, D.G. A quantitative analysis of the dendritic organization of pyramidal cells in the rat hippocampus. *J. Comp. Neurol.* **362**, 17–45 (1995).
47. Melzer, S. *et al.* Long-range-projecting GABAergic neurons modulate inhibition in hippocampus and entorhinal cortex. *Science* **335**, 1506–1510 (2012).
48. Contractor, A., Swanson, G.T., Sailer, A., O'Gorman, S. & Heinemann, S.F. Identification of the kainate receptor subunits underlying modulation of excitatory synaptic transmission in the CA3 region of the hippocampus. *J. Neurosci.* **20**, 8269–8278 (2000).
49. Berzhanskaya, J., Urban, N.N. & Barrionuevo, G. Electrophysiological and pharmacological characterization of the direct perforant path input to hippocampal area CA3. *J. Neurophysiol.* **79**, 2111–2118 (1998).
50. MacDonald, C.J., Lepage, K.Q., Eden, U.T. & Eichenbaum, H. Hippocampal "time cells" bridge the gap in memory for discontiguous events. *Neuron* **71**, 737–749 (2011).

ONLINE METHODS

Experiments were conducted in accordance with the Massachusetts Institute of Technology Department of Comparative Medicine and approved by the committee on Animal Care (CAC). Mice were housed 2–5 littermates per cage with a regular dark-light cycle, with water and food provided *ad libitum*. Post-surgery mice were individually housed.

Immunohistochemistry. Adult mice were transcardially perfused with 4% (wt/vol) paraformaldehyde (PFA) in phosphate-buffered saline (PBS). The brains were then post-fixed by the same solution for 24 h, processed in 30% (wt/vol) sucrose in PBS and embedded in an OCT compound (Sakura). Brains were frozen with dry ice and sectioned by cryostat (50-μm-thick sagittal sections).

For RGS14, PCP4 and STEP staining, freely floating sections were incubated with 3% (vol/vol) goat serum in 0.3% (vol/vol) Triton-X PBS (PBS-X) for 1 h. Sections were then incubated with primary antibodies (mouse isotype2a antibody to RGS14, 1:500, 75-170, NeuroMAB; rabbit antibody to PCP4, 1:200, HPA005792, Sigma-Aldrich; mouse isotype1 antibody to STEP, 1:500, 4396S, Cell Signaling Technology) in 3% goat serum in 0.3% PBS-X overnight at 4 °C. After rinsing three times with PBS-X for 15 min, sections were incubated with secondary antibodies (antibody to mouse isotype1 conjugated to Alexa 488, 1:200, A21121, Invitrogen; antibody to mouse-isotype2a conjugated to Alexa 555, 1:200, A21137, Invitrogen; antibody to rabbit conjugated to CF633, 1:200, 20123, Biotium) in PBS-X with 3% goat serum for 2 h at room temperature 23 °C.

For PCP4 and calbindin staining and PCP4 and GAD67 staining, sections were visualized using primary antibodies (rabbit antibody to PCP4, 1:200, HPA005792, Sigma-Aldrich; mouse antibody to calbindin, 1:500, 300, Swant; mouse antibody to GAD67, 1:500, MAB5406, Millipore) and by secondary antibodies (antibody to rabbit Alexa 488, 1:200, A11034, Invitrogen; antibody to mouse Alexa 555, 1:200, A21424, Invitrogen).

For actinin2 and PCP4 staining, sections were visualized using primary antibodies (rabbit antibody to PCP4, 1:200, HPA005792, Sigma-Aldrich; mouse antibody to α-actinin2, 1:200, A7811, Sigma-Aldrich) and by secondary antibodies (antibody to rabbit Alexa 488, 1:200, A11034, Invitrogen; antibody to mouse Alexa 555, 1:200, A21424, Invitrogen).

For RGS14 and WFS1 staining, sections were visualized using primary antibodies (mouse antibody to RGS14, 1:500; rabbit antibody to WFS1, 1:250, 11558-1-AP, ProteinTech Group) and secondary antibodies (antibody to mouse Alexa 488, 1:200, antibody to rabbit Alexa 555, 1:200).

For ZnT3, VGluT1 and RGS14 staining, sections were visualized using primary antibodies (rabbit antibody to ZnT3, 1:500, 197 002, sysy; Guinea pig antibody to VGluT1, 1:1,000, AB5905, Millipore; mouse antibody to RGS14, 1:500) and secondary antibodies (antibody to rabbit Alexa 488, 1:200; antibody to guinea pig Alexa 555, 1:200, A21435, Invitrogen; antibody to mouse CF633, 1:200, 20121, Biotium).

For ZnT3, PSD95 and RGS14 staining, sections were pre-treated with antigen retrieval solution (pepsin, GTX28194, Gene Tex) at 37 °C for 15 min. Sections were then visualized using primary antibodies (guinea pig antibody to ZnT3, 1:500, 197 004, sysy; rabbit antibody to PSD95, 1:500, Rb-Af628, Frontier Institute; mouse antibody to RGS14, 1:500) and secondary antibodies (antibody to guinea pig Alexa 488, 1:200, A11073, Invitrogen; antibody to rabbit Alexa 555, 1:200; antibody to mouse CF633, 1:200)

For PCP4 and BDA staining, sections were incubated with 5% (vol/vol) goat serum, followed by 3% (vol/vol) goat serum with 1% (vol/vol) goat antibody to mouse FAB fragment (115-007-003, Jackson ImmunoResearch Laboratory) in PBS-X for 1.5 h (serum with FAB blocking). After rinsing with PBS-X for 15 min three times, sections were visualized using primary antibodies (rabbit antibody to PCP4, 1:200) and secondary antibodies (antibody to rabbit Alexa 488, 1:200; streptavidin Alexa 555, 1:200, S32355, Invitrogen).

For HSV experiment, after blocking with serum and FAB, the sections were visualized using primary antibodies (antibody to RGS14, 1:300, chicken antibody to GFP antibody, 1:500, A10262, Invitrogen) and secondary antibodies (antibody to chicken Alexa 488: 1:200, A11039, Invitrogen, antibody to mouse CF633: 1:200).

For RGS14, ArchT-GFP and synaptororin staining, after blocking with serum and FAB, sections were visualized using primary antibodies (mouse antibody to RGS14, 1:300; chicken antibody to GFP, 1:500, Invitrogen; rabbit antibody to synaptoporin, 1:500, 102 002, sysy) and secondary antibodies (antibody to

mouse Alexa 555, 1:200; antibody to chicken Alexa 488, 1:200; antibody to rabbit CF633, 1:200, Biotium).

For Prox1 staining in DGGCs, RGS14 staining in CA3 Cre transgenic mice and CA2 Cre knock-in mice, and PCP4 staining in CA2 Cre knock-in mice, after blocking with serum and FAB, sections were visualized using each primary antibody (mouse antibody to Prox1, 1:250, P21936, Invitrogen; mouse antibody to RGS14, 1:300; rabbit antibody to PCP4, 1:200) and secondary antibody (antibody to mouse Alexa 555, 1:200; antibody to rabbit Alexa 555, 1:200).

For entorhinal cortex–specific histology, sections were visualized using primary antibodies (antibody to RGS14, 1:150 NeuroMab, calbindin, 1:1,000, Abcam, and netrin-G2, 1:5,000, ref. 34) and secondary antibodies (goat antibody to mouse Alexa 555, goat-antibody to mouse Alexa 633, goat-antibody to rabbit 555 or goat-antibody to rabbit 488, 1:500, Invitrogen).

All sections were incubated with DAPI (1:5,000, stock solution of 1 mg ml^{-1}, Invitrogen) for 15 min and mounted on glass slides. For all representative images displayed in the figures, experiments were successfully repeated more than three times.

Diolistic labeling. Mice were transcardially perfused with 1.5% (wt/vol) PFA in PBS, and the brains were postfixed by the same solution for 1 h. Then, 150-μm-thick sections were prepared by a vibratome and labeled by using Gene-gun (Bio Rad) and Dil-labeled tungsten particles (1.3 μm, Bio Rad). After 24 h at room temperature (23 °C, sections were incubated with 5% goat serum in 0.1% PBS-X for 1 h, then incubated with antibody to RGS14 (1:500) in 3% goat serum 0.05% PBS-X for 16 h, and visualized using antibody to mouse Alexa 488 (1:200).

Generation of DGGC-specific transgenic Cre mice. The bacterial artificial chromosome (BAC) modification was carried out using BAC recombineering technology. The BAC clone RP23-153B7 (210 kb), including the *Dock10* promoter and gene, was transferred to the EL250 bacterial strain. The Cre sequence was inserted in-frame into the second exon shared by the major Dock10 isoforms. The BAC modifying cassette consisted of a 5′ homology arm, the Cre coding region in-frame with *Dock10* second exon sequence, the kanamycin resistant gene flanked by FRTs, and a 3′ homology arm. The purified BAC modifying cassette was electroporated into the EL250 containing the RP23-153B7 BAC, and screened by PCR and Southern hybridization. Kanamycin resistant gene was removed by FLPe recombinase integrated into the EL250 genome. PFGE and fingerprinting analysis using BamHI and EcoRI restriction enzymes were carried out to confirm the correct modification of the BAC clone. The purified BAC DNA including the transgene was linearized by *Not*I restriction enzyme, and the vector backbone part was removed. The purified BAC insert was microinjected into fertilized eggs (C57BL/6J) at the pronuclear stage. Successfully developed two cell–stage embryos were transferred to pseudopregnant recipient females of Jcl:ICR (Clea Japan). The germline transmission was confirmed by PCR.

Generation of CA2-specific knock-in Cre mice. PGK-NeoF2L2DTA was used as a backbone vector to build the knock-in Cre construct. The 5′ homology arm (5 kb) was PCR amplified from BAC (RP24-211E22) by a forward primer, including the NotI site, and the reverse primer, including AatII+SalI site. This 5′ homology arm was inserted into NotI-SalI site of PGK-NeoF2L2DTA. The 3′ homology arm (5 kb) was PCR-amplified from BAC (RP24-211E22) by forward primer including AatII+MluI sites and reverse primer including SalI site. The 3′ homology arm was inserted into the AatII-SalI site of backbone vector. Transgene cassettes consisted of NaeI-T2A peptide-Cre–rabbit b-globin polyA–FRT-Neo cassette-FRT-MluI.

T2A peptide is a self-cleaving peptide. The amino acid sequence of T2A peptide was GSGEGRGSLLTCGDVEENPGPAPGS. Restriction-digested T2A-Cre-polyA-FRT-Neo cassette-FRT fragment was inserted into the blunted AatII-MluI site between the 5′ homology arm and the 3′ homology arm. T2A-Cre-polyA-FRT-Neo cassette-FRT was inserted immediately before the STOP codon of Map3k15. The vector was linearized by NotI and electroporated into embryonic stem cells (C57BL/6 background, inGenious Targeting Laboratory). Positive clones were confirmed and selected by PCR and Southern-blot analysis. Positive embryonic stem cells were injected into blastocysts of BALB/C mice to generate chimeric mice. Germline transmission of transgene was confirmed by PCR.

Generation of viruses. The HSV-1 amplicon vector including mini-Penk promoter (2753bp) and ChETA-YFP was created. HSV-miniPenk-ChETA-YFP

was packaged in the Viral Gene Transfer Core at the Massachusetts Institute of Technology. The ArchT-GFP transgene was PCR-amplified and inserted into the AAV-TRE backbone vector. AAV9-TRE-ArchT-GFP was packaged at UMASS. tTA2 was PCR-amplified from Tet-Off advanced vector (clonthech) and inserted into AscI-NheI site in pAAV-EF1a-DIO-ChR2-YFP vector. Then, DIO-tTA transgene fragment was digested by BamHI and EcoRI, and inserted into BamHI-EcoRI site of FCK(1.3)-NPHR-TS-EYFP-ER vector. Lentivirus-CamKIIα (1.3kb)-DIO-tTA was packaged at UMASS. AAV9-EF1a-DIO-ChR2-YFP was generated by UPENN (AV-9-20298P). R. Neve (Viral Vector Core Lab, Massachusetts Institute of Technology) generated the AAV8-CMV-Synaptophysin-mCherry virus, with a titer of 2.1×10^{13} genome copies per ml. CaMKIIa-ChR2-YFP (Addgene #26969) was cloned and generated as an AAVrh8 virus at the UMASS Vector Core Gene Therapy Center with a titer of 8.0×10^{12} genome copies per ml.

Stereotaxic injections from bregma. Mice were anesthetized with isoflurane and placed into a stereotaxic frame. Hamilton syringe with a 26-gauge needle was used for viral injection. All viruses were injected in the right hemisphere of the mouse brain at the following coordinates relative to bregma.

To trace SUM projections, we injected 70 nl of biotinylated dextran amine (concentration 0.1 mg μl^{-1} in 0.1× PBS, Invitrogen, MW 10,000) into the SUM of adult mice at +0.14 mm ML, −2.85 mm AP and −4.86 mm DV (ML, mediolateral; AP, anteroposterior; DV, dorsoventral) and perfused the mice after 6 d.

To obtain sparsely labeled mossy fiber terminals, we injected 1,000 nl of HSV-miniPenk-ChETA-YFP (titer = 4×10^8) in the dentate gyrus of adult wild-type mice at +0.60 mm ML, −1.78 mm AP and −2.30 mm DV and perfused the mice after 2 d.

To label the dentate longitudinal projections along CA2, we injected 200 nl of 3:1 AAV9.ArchT/Lenti.TTA mixed solution (AAV9 titer = 1.5×10^{13}, Lenti titer = 10^{10}) in the dentate gyrus of adult DGGCs Cre mice at +0.45 mm ML, −1.34 mm AP and −2.20 mm DV, or, to label more caudal mossy fiber longitudinal projections, we injected 100 or 200 nl of the same solution in the dentate gyrus of adult DGGCs Cre mice at +2.26 mm ML, −3.08 mm AP and −2.5 mm DV and perfused the mice after 9 d.

For optogenetics and histology of DGGCs, we injected 100 nl of AAV9.EF1a. DIO.ChR2 (titer = 2.56×10^{13}) in the dentate gyrus of 4-week-old DGGCs Cre male mice at +1.00 mm ML, −2.00 mm AP and −2.05 mm DV and killed the mice after 4 d.

For optogenetics and histology of CA2, we injected 100 nl of AAV9.EF1a. DIO.ChR2 (titer = 0.85×10^{13}) in CA2 of 4–5-week-old female CA2 Cre mice at +1.95 mm ML, −1.82 mm AP and −1.7 mm DV and killed the mice after 5 d.

For histology of CA3, we injected 100 nl of AAV9.EF1a.DIO.ChR2 (titer = 1.28×10^{13}) in the CA3 of 7–8-week-old male and female CA3 Cre mice at +2 mm ML, −1.7 mm AP and −2.12 mm DV and perfused the mice after 6 d.

For optogenetics of CA3, we injected 100 nl of AAV9.EF1a.DIO.ChR2 (titer = 1.28×10^{13}) in the CA3 of 4–5-week-old male and female CA3 Cre mice at +2 mm ML, −1.7 mm AP and −2.12 mm DV and killed the mice after 6 d.

For morphological study of CA2, we injected 100 nl of AAVRh8.synapsin. DIO.TVA-2A-GFP-2A-B19G (AAV-DIO-sTpEpG) (titer = 2.29×10^{12}) in the right CA2 of adult CA2 Cre-mice at the following stereotaxic coordinates (from bregma): +1.95 mm ML, −1.82 mm AP and −1.7 mm DV and perfused the mice after 7 d.

For morphological analysis of EC-III/EC-II fibers into the hippocampus, 4-week-old *pOxr1* mice were injected with 700 nl AAV9-EF1α-DIO-ChR2-YFP or with a 1:1, 400-nl mixture of AAV9-EF1α-DIO-ChR2-YFP and AAV8-CMV-Synaptophysin-mCherry at +3.35 mm ML, −4.7 mm AP and −3.30 mm DV for MEC and +4.3 mm ML, −3.4 mm AP and −4.00 mm DV for LEC and killed after 7 d.

For optogenetic stimulation of entorhinal cortex fibers, 3-week-old *pOxr1*-Cre mice were injected with 700 nl of AAV9-EF1α-DIO-ChR2-YFP or 500 nL of AAVrh8-CaMKIIa-ChR2-YFP at +3.35 mm ML, −4.7 mm AP and −3.30 mm DV and killed after 7 d.

Fluorescence imaging. All fluorescence images were taken by confocal microscopy (Zeiss LSM700 or Olympus FV1000) using 10×, 20×, 40×, 63× objectives and by fluorescent microscopy (Zeiss Axioimager Z1) using 10×, 20× objectives. Z-projected confocal images were generated by Fluoview viewer (Olympus) and Zenblack (Zeiss).

Analysis of the overlay between CA2 markers. To analyze the overlay between CA2 markers, images centered on the CA2 region, were acquired by confocal microscopy on a sample stained with antibodies to RGS14, PCP4 and STEP or antibody to α-actinin2. The RGS14-positive cells were identified on a single focal plane and visually inspected for coexpression (n = 6 mice, cell number per sample: maximum = 42, minimum = 28, mean = 34 ± 2).

To test the targeted expression of ChR2-YFP in the CA2 cell–specific Cre mice, we analyzed the overlay between ChR2-YFP–positive cells and PCP4. A sequential series of images, centered on the CA2 region, were acquired by confocal microscopy (n = 12 images per sample every 1.2 μm) of a sample expressing YFP and stained with antibody to PCP4. The ChR2-YFP–positive cells were identified on a single focal plane and visually inspected for coexpression with PCP4 (n = 3 mice, cell number per sample: maximum = 60, minimum = 25, mean = 42 ± 10). CA3 or CA1 pyramidal cells were all ChR2-YFP negative.

Identification of CA2 pyramidal cells overlapped by mossy fibers. A sequential series of images were acquired by confocal microscopy (15 images per sample every 1.5 μm). Mossy fibers were stained with antibody to calbindin and CA2 pyramidal cells by antibody to PCP4. All the PCP4-positive cells were selected by identification on a single focal plane. The border between CA2 cells overlapped by mossy fibers and CA2 cells not overlapped by mossy fibers was established by using a line parallel to the apical dendrites and intercepting the distal end of the mossy fibers. The percentage of CA2 neurons overlapped by mossy fibers was 82.2 ± 1.06% and that non-overlapped by mossy fibers was 17.8 ± 1.06% (n = 5 mice; **Fig. 2a,b**).

Measurement of mossy fiber terminal (MFT) diameter. To measure the MFT diameter, we infected dentate granule cells with HSV mini-Penk promoter-ChETA-YFP, obtaining sparsely labeled mossy fibers. A sequential series of images centered, for each sample, on the stratum lucidum of CA2 and CA3a/b was acquired every 0.5 μm by confocal microscopy (LSM700, Zeiss). Measurements were obtained off-line using the Zenblack software (Zeiss) on a $20 \times 20 \times 7$ μm^3 region selected, for each sample, in the stratum lucidum of both CA2 and CA3a/b. YFP-positive MFT were identified as varicosities located in the stratum lucidum, arranged either *en passant*, or as side structures connected to the mossy fiber projection by side-branches and characterized by a diameter ranging 0.5–4 μm (axon diameter ~0.3 μm). *En passant* terminals diameter were measured on the axis perpendicular to the direction of terminal, whereas, for side structures, the diameter was measured on the axis perpendicular to the side branch.

Analysis of the longitudinal septotemporal component of mossy fibers. The extent of the longitudinal component of mossy fibers in CA2 was estimated by injecting a AAV9.ArchT/Lenti.TTA mixed solution in the dentate gyrus of adult DGGCs Cre mice. Viruses were injected in the dorsal (ML: +2.26 AP: −3.08 DV: −2.50, n = 3 mice), intermediate (ML: +2.70 AP: −2.72 DV: −3.30, n = 3 mice) or in the ventral (ML: +3.15 AP: −3.3 DV: −4.10, n = 3 mice) dentate gyrus of the hippocampus. We obtained sparsely GFP-labeled dentate granule cells allowing us to follow GFP-positive mossy fibers along the septotemporal axis of the hippocampus. Fluorescence and confocal images were acquired from septotemporal sagittal hippocampal sections (for dorsal injections) or horizontal sections (for intermediate and ventral injections). Analysis was performed on a series of fluorescence images by targeting the CA2 region, labeled by RGS14. Fluorescence intensity was measured within a region of interest (20×20 μm) located into the CA2 stratum lucidum (SL). Background fluorescence was measured by setting another region of interest in the CA2 stratum radiatum (SR). Data are presented as normalized fluorescence intensities: $SL_{FLUORESCENCE} / SR_{FLUORESCENCE}$.

Tissues (n = 6) from three adult DGGCs Cre mice infected with AAV9.ArchT/Lenti.TTA mixed solution were acquired by confocal microscopy to count the number of MFT in the distal CA3 RGS14-negative region and in the CA2 RGS14-positive region in the longitudinal component of mossy fibers.

Mice and slice preparation. Mice were anesthetized by isoflurane and decapitated, and their brains were removed. By using an oxygenated cutting solution at ~4 °C, 300-μm-thick sagittal slices were prepared with a vibratome (VT1000S, Leica). Slices were then incubated at ~23 °C in oxygenated artificial cerebrospinal fluid (ACSF) until the recordings. The cutting solution contained 3 mM KCl, 0.5 mM $CaCl_2$, 10 mM $MgCl_2$, 25 mM $NaHCO_3$, 1.2 mM NaH_2PO_4, 10 mM D-glucose, 230 mM sucrose, saturated with 95% O_2/5% CO_2 (pH 7.3, osmolarity

340 mOsm). The ACSF contained 124 mM NaCl, 3 mM KCl, 2 mM CaCl$_2$, 1.3 mM MgSO$_4$, 25 mM NaHCO$_3$, 1.2 mM NaH$_2$PO$_4$, 10 mM D-glucose, saturated with 95% O$_2$/5% CO$_2$ (pH 7.3, osmolarity 300 mOsm). Slices were transferred into a submerged experimental chamber and perfused with oxygenated 36 °C ACSF at a rate of 3 ml min^{-1}.

Electrophysiology. Whole-cell recordings in current-clamp or voltage-clamp mode were performed by using an infrared differential interference contrast microscope (BX51, Olympus) with a water immersion 40× objective (N.A. 0.8), and equipped with four automatic manipulators (Luigs & Neumann) and a CCD camera (Orca R2, Hamamatsu). Borosilicate glass pipettes were fabricated (P97, Sutter Instrument) with resistances of 8–10 MΩ, and filled with the following intracellular solution 110 mM potassium gluconate, 10 mM KCl, 10 mM HEPES, 4 mM ATP, 0.3 mM GTP, 10 mM phosphocreatine and 0.5% (wt/vol) biocytin (pH 7.25, osmolarity 290 mOsm). Access resistance was monitored throughout the duration of the experiment and data acquisition was suspended whenever the resting membrane potential was depolarized above –50 mV or the access resistance was beyond 20 MΩ. Recordings were amplified using up to two dual channel amplifiers (Multiclamp 700B, Molecular Devices), filtered at 2 kHz, digitized (20 kHz) and acquired using custom made software running on Igor Pro (Wavemetrics).

Optogenetics. Optogenetic stimulation was achieved through a 460-nm LED light source (XLED1, Lumen Dynamics) driven by TTL input with a delay onset of 25 µs (subtracted off-line). Light power on the sample was 33 mW mm^{-2}, and only the maximum power was employed. Slices were stimulated by single 2-ms light pulse repeated 30 times every 4 s or train of 15 light pulses at 30 Hz repeated 20 times every 6 s. In voltage-clamp cells were held at –70 mV for EPSC measurements, whereas, in current mode, EPSP and action potentials were measured at resting potentials. Pharmacological compounds were obtained from Tocris. For optogenetic stimulation of mossy fibers, CA1, CA2 and CA3 cells were sequentially recorded in the same slice. For optogenetic stimulation of CA2 or CA3 terminals, CA1 pyramidal cell pairs, one deep and one superficial cell, were sequentially recorded in the same slice, less than 100-µm intersomatic distance. For stimulation of MECII fibers, to avoid potential polysynaptic contamination of the postsynaptic response through the dentate gyrus, we made a micro-scissor cut through the mossy fibers.

Analysis. The intrinsic electrophysiological properties were measured current mode, the cell at –70 mV. Input resistance was estimated by linear fit of the *I-V* relationship (injection of 10–12 current steps of 1-s duration). Action potential threshold was tested with a current ramp injection. Membrane time constant was estimated through single exponential fit of the recovery-time from a –100 pA current step injection of 1-s duration. Sag amplitude was measured in response to a 1-s negative current step pulse reaching –100 mV. Synaptic connections, in voltage or current mode, were determined by averaging 30 trials.

EPSC amplitude was measured from the average maximum peak response by subtracting a baseline obtained 5 ms before light pulse starts. EPSC onset was measured from the beginning of the light pulse to the starting point of the response estimated through the intercept between the baseline and a parabolic fit of the rising phase of the EPSC. Action potential peak time was measured from the beginning of the light pulse to the maximum peak of the action potential.

Statistics. Statistical analysis was performed using Igor (Wavemetrics), Matlab (Mathworks) or Excel (Microsoft). Sample size, estimated with Mead's resource equation, was adequate to reveal a strong statistical effect and sufficient to avoid unnecessary animal sacrifices. There was no explicit blinding or randomization. The distribution of the data was tested with the Kolmogorov-Smirnov test. A two-tailed paired or unpaired *t* test was employed for comparison. Data are presented as mean ± s.e.m.

Post hoc **immunocytochemistry after recording.** Recorded slices were recovered for morphological identification as the recorded cells were filled with biocytin. For dentate gyrus–CA2 experiments, slices were first incubated with 4% PFA in PBS for 16 h at 4 °C and then incubated with 5% goat serum for 1 h, followed by 3% goat serum with 1% antibody to mouse FAB fragment in 0.5% PBS-X for 1.5 h. After washing with 0.5% PBS-X for 15 min, slices were incubated with primary antibodies (mouse antibody to RGS14, 1:300) for 16 h

and visualized by antibody to mouse Alexa 555 (1:200) and Streptavidin CF633 (1:200, 29037, Biotium). Slices were also incubated with DAPI (1:5,000) for 15 min before mounting. Only pyramidal cells located in the CA2 region and expressing RGS14 were considered CA2 pyramidal cells. For dentate gyrus–CA2 interneurons experiments, slices were visualized using primary antibody (mouse antibody to GAD67, 1:250, MAB5406, Millipore; rabbit antibody to parvalbumin, 1:250, ab11427, Abcam) and secondary antibody (antibody to mouse CF405, 1:200, 20080, Biotium; antibody to rabbit Alexa 555, 1:200; streptavidin CF633, 1:200). For CA2-CA1 and CA3-CA1 experiments, after the same fixing and blocking treatment, slices were incubated with primary antibodies (mouse antibody to CaMKIIα, 1:300, ab22609, Abcam; rabbit antibody to calbindin, 1:800, ab11426, Abcam) in 0.5% PBS-X for 16 h and visualized by antibody to mouse CF405 (1:200, Biotium), antibody to rabbit Alexa 555 (1:200) and Streptavidin CF633 (1:200). Only pyramidal cells whose cell bodies were located in the superficial CA1 sublayer and expressing CaMKIIα and calbindin were considered as superficial CA1 pyramidal cells. Only pyramidal cells whose cell bodies were located in the deep CA1 sublayer and expressing CaMKIIα, but not calbindin, were considered as deep CA1 pyramidal cells.

Estimation of channelrhodopsin-2 expression across different mouse lines. All experiments performed in brain tissues infected with AAV9-EF1a-DIO-ChR2-YFP viruses, fully expressed channelrhodopsin-2 at a saturated level. For the four cell type–specific Cre mouse lines used in this study (dentate gyrus, CA2, CA3 or MECIII specific), the channelrhodopsin-2 expression was quantified selecting a region of interest of 0.3 × 0.3 µm on the axonal terminals and analyzing the native fluorescence intensity expressed by the axonal terminals (ChR2-YFP). By comparing fluorescence intensities across mouse lines, no significant differences were detected.

Monosynaptic tracing with rabies virus. For the rabies virus experiments, an AAV vector for Cre-dependent simultaneous expression of the three genes encoding TVA, EGFP and the rabies virus glycoprotein (RVG) was constructed as follows. The sequence between the inverse terminal repeats of pAAV-MCS (Stratagene) was deleted in its entirety and replaced with a cassette consisting of: 1, the human synapsin-1 promoter (*SYN1*, Genbank NG_008437); 2, a synthesized construct consisting of a Kozak sequence and the initial codons of TVA interrupted by a FLEX cassette designed so as to constitute a complete open reading frame after Cre recombination, following a strategy devised to avoid leaky expression of TVA; 3, within the FLEX cassette, inverted with respect to the promoter, a sequence consisting of three genes—in frame with each other and separated by the highly efficient porcine teschovirus self-cleaving 2A elements—encoding the transmembrane isoform of TVA (lacking a start codon), EGFP, and RVG; 4, the woodchuck post-transcriptional regulatory element and bovine growth hormone polyadenylation site. Gene synthesis and the majority of cloning steps were performed by Epoch Life Science. This genome was packaged into AAV serotype rh.8 capsids by the University of Pennsylvania Vector Core. A key difference of this newly constructed AAV versus the similar and widely used pAAV-EF1a-FLEX-GTB (Addgene #26197) is the reduction of the total length of the genome to 4.7 kb (within the established packaging limit of AAV), which we achieved by using a much smaller promoter and polyadenylation signal and by removal of all extraneous sequences and restriction sites.

Deletion-mutant rabies virus was produced by replacing the EGFP gene in cSPBN-4GFP with the gene encoding mCherry. Packaging with the ASLV-A envelope protein was made as previously described.

For the monosynaptic tracing experiment, 50 nl of AAV-synP-FLEX-sTpEpB was stereotaxically delivered into the dorsal CA2 region of *Map3k15-cre* or C57BL/6NTac mice (ML, +1.95; AP, –1.82; DV, –1.7). Experiments were all conducted in 14–18-week-old male mice. 7 d after AAV injection, 50 nl of rabies virus, RVΔG-mCherry(EnvA), was injected at the same coordinates, and mice were killed 7 d later. We noticed no starter cells outside of the CA2 area. As a negative control, we applied the same experimental procedure to wild-type C57BL/6NTac mice and observed neither an EGFP signal nor any mCherry signal outside of the virus injection site. Around the injection area, we did observe a small number of both EGFP and mCherry-positive cells. This is presumably a result of some combination of nonzero tropism of EnvA for mammalian cells, the presence of residual 'unpseudotyped' rabies virus and potentially nonzero expression of TVA from the AAV in the absence of Cre (**Supplementary Fig. 15**).

Rabies virus mCherry-positive cell counting in the entorhinal cortex. To discriminate layer II and layer III neurons in the MEC and LEC expressing mCherry, horizontal sections were stained by NeuroTrace 640/660 for Deep-Red Fluorescent Nissl Stain (Invitrogen, N-21483). After Nissl staining, we analyzed the distributions of rabies virus-labeled, mCherry-only positive cells in layer II and layer III of MEC and LEC by using Zeiss ZEN software (Zeiss). The determination of MEC and LEC, as well as of layer II and layer III, was guided by the criteria previously used. We examined a total of 18 slices from three mice. In regions in which mCherry-positive cells were observed, we counted the total number of mCherry-positive cells in each layer and divided it by the estimated total number of cells in that layer. The total number of mCherry-only positive cells in LEC and MEC was 426 and 698, respectively. To estimate the total number of cells in each layer, we measured the relative volume of each layer and then estimated the total number of cells in each of those layers. We counted all Nissl positive cells in a $100 \times 100 \times 30$ µm confocal stack of the layer II and layer III regions for MEC and LEC of each animal. From this count, we estimated the total number of cells in MEC-II, MEC-III, LEC-II and LEC-III selected regions for each animal.